



School of Mechanical and Manufacturing Engineering

Faculty of Engineering

The University of New South Wales

Wingtip Pressure Distribution Measurements

by

Moshe Meir Hollander

Thesis submitted as a requirement for the degree of
Bachelor of Aerospace Engineering

Submitted: June 2018

Student ID: z3373926

Supervisor: Dr Danielle Moreau

ORIGINALITY STATEMENT

'I hereby declare that this submission is my own work and to the best of my knowledge it contains no materials previously published or written by another person, or substantial proportions of material which have been accepted for the award of any other degree or diploma at UNSW or any other educational institution, except where due acknowledgement is made in the thesis. Any contribution made to the research by others, with whom I have worked at UNSW or elsewhere, is explicitly acknowledged in the thesis. I also declare that the intellectual content of this thesis is the product of my own work, except to the extent that assistance from others in the project's design and conception or in style, presentation and linguistic expression is acknowledged.'

Signed 

Date 28/05/2018

Abstract

Few if any studies have been conducted in order to measure mean or surface pressure at the tip region of the airfoil. A series of NACA 0012 models, with a chord length of 0.08m and an aspect ratio of 1 have been constructed in order to carry out such tests. Mean and fluctuating pressure have been recorded throughout a range of flow conditions, with Re ranging between $0.25 \cdot 10^5$ to $2.04 \cdot 10^5$, and α ranging between 0° and 20° . Mean pressure measurements along the front of the airfoil indicate sharp attachment and reattachment phenomena occurring between $x/c=0.2$ and $x/c=0.5$. Along the suction and pressure sides of the tip region, marked deviations from the mean pressures suggested by 2D airfoil theory indicates the presence of strong 3D flow effects, and potentially indicates high levels of turbulence. Unsteady pressure data reveals a strong relationship between pressure spikes at high frequencies at the surface, and free-field acoustic data presented in literature. Further analysis of this data indicates a relationship between the total power output of the turbulence within this region, and angle of attack, which in turn relates to an increase in the magnitude of macro level flow phenomena along with angle of attack. This work can serve as the basis for higher fidelity experimental work, as well as validation for CFD studies.

Acknowledgements

First and foremost, I would like to thank my supervisor Dr. Danielle Moreau for her expert guidance and encouragement throughout the writing of this thesis. Thanks is also owed to Dr. Manuj Awasthi and Omead Saeed for assisting me in the operation of key pieces of lab equipment and analysis procedure guidance. I am also very grateful for the tireless efforts of Benjamin Willis who worked his 3D printing magic in record time.

I would also like to thank my proof-reading volunteer Naomi Ehrenkranz, without whom this thesis would be practically indecipherable.

Lastly, I would like to thank my parents, my eternal cheerleaders, whose love, kindness and unyielding belief in me have played no small part in any success that I can claim.

Nomenclature

b	wingspan (m)
c	chord length (m)
L	Line increment directed along vortex
R	Separation between points on vortices
U	Local fluid velocity ($\frac{m}{s}$)
x	chord-wise axis
y	span-wise axis
C_L	coefficient of lift
C_D	coefficient of drag
CFD	Computational Fluid Dynamics
dB	Decibels
dBA	A-Weighted decibel level
$G(\omega)$	Power spectral density (as a function of frequency)
LES	Large Eddy Simulation
PIV	Particle Image Velocimetry
Re	Reynolds Number
U_∞	Freestream velocity
St	Strouhal number $\frac{fc}{V_\infty}$
α	angle of attack ($^\circ$)
Γ	Circulation around a vortex
Γ_0	Circulation at large radius

Contents

1	Introduction	1
2	Background	2
2.1	Literature Review	2
2.1.1	Background Motivation Literature	3
2.1.2	Theoretical Models	5
2.1.3	Experimental Far-Field Vortex Studies	6
2.1.4	Computational Far-Field Vortex Studies	13
2.1.5	Experimental Near-Field Vortex Studies	14
2.1.6	Numerical Near-Field Vortex Studies and Surface Pressure Measurements	22
2.1.7	Summary	22
3	Aims and Methodology	23
3.1	Aims	23
3.2	Methodology	24
3.2.1	Facilities	24
3.2.2	Test Geometry	24
3.2.3	Test Matrix	33
4	Results and Discussion	34
4.1	Results	34
4.1.1	Mean Pressure Measurements	34
4.1.2	Fluctuating Pressure Results	41
5	Conclusion	45
5.1	Future Work	46
	Bibliography	47
	Appendix A	50
	Appendix B	53
B.1	MATLAB code used to gather and analyse mean pressure data . .	53

B.2	MATLAB code used to compute and plot the RMS values of the spectral data	54
Appendix C		56
C.1	y/c sweep data near the tip region	56

List of Figures

2.1	Photographs of wake at various stations behind a triangular wing of aspect ratio 2. $\alpha = 12^\circ$, $CL \approx 0.55$	7
2.2	Photographs of vortex core dissipation in calm air.	8
2.3	Extended near field vortices evolution. The dark shaded regions indicate areas of higher vorticity.	9
2.4	Vortex paths varying AoA (y-x plane)	10
2.5	Nondimensional axial velocity distributions (\bar{u}/U_∞) at $x/b=0.5$ for $\alpha = 8^\circ$, $\alpha = 15^\circ$. Note, WLW = ‘Wing Leading-Edge Vortex’, WTV = ‘Wing Trailing-Edge Vortex’, CLV = ‘Canard Leading-Edge Vortex’, and CTV = ‘Canard Trailing-Edge Vortex.	11
2.6	Circulation parameter as a function of angle of attack: flat and rounded end-cap data are represented by solid and open symbols, respectively.	12
2.7	Contour plots of nondimensional axial vorticity (denoted here as ξ) at various points downstream of the model.	14
2.8	Projection of streamlines in the crossflow plane, wing tip region, $\alpha = 4^\circ$, $Re = 2.47 \cdot 10^5$. Of particular note, is the initial formation of the secondary vortex at $x/c = 0.05$	15
2.9	Typical normalized vorticity contours for $\alpha = 10^\circ$. [1]	17
2.10	An example of a normalised velocity contour plot presented in the study. $x/c=0.8$	18
2.11	Vortex at $Re=3000$, $\alpha = 12^\circ$ on rounded tip; wing section in gray.	19
2.12	Axial velocity at $Re=7.4 \cdot 10^5$, $\alpha = 12^\circ$	19
2.13	Laser light sheet flow visualization of a fully developed blade tip vortex where ‘1’ shows the inner zone free of large turbulent eddies, ‘2’ shows a transitional region with eddies of different scales, and ‘3’ shows an outer, essentially potential flow region.	20
3.1	Benchtop wind tunnel model AF1125, manufactured by TECQUOP-MENT.	24
3.2	Coordinate definition, x-z	25

3.3	Model mount component, to be screwed into the tunnel wall. . . .	25
3.4	'Front-Tapped' attachment.	26
3.5	'Top-Tapped' attachment.	26
3.6	Example of assembly: This is an image of the 'front' taps attachment being attached to the 'base'.	29
3.7	The 'front' taps and 'base' fully assembled and installed within the wind tunnel. Note that the 'top' and 'base' have been secured together using speed tape, and the whole assembly has been secured to the test section 'floor' using speed tape.	29
3.8	Diagram illustrating the placement of the model assembly within the tunnel test section.	30
3.9	Broader view of calibration setup. Note the cradle in which the microphones sit (used during measurement as well as calibration) and the connection between the cradle outputs and the model taps.	32
3.10	Close up, birds-eye view of the calibration setup. Note the perpendicular positioning of the a)reference speaker, b)reference microphone, and the model taps.	33
4.1	Mean pressure on 'front' surface. Angle sweep at $10 \frac{m}{s}$, $Re = 5.102 \cdot 10^4$	35
4.2	Mean pressure on 'front' surface. Angle sweep at $20 \frac{m}{s}$, $Re = 1.020 \cdot 10^5$	36
4.3	Mean pressure on 'front' surface. Angle sweep at $30 \frac{m}{s}$, $Re = 1.531 \cdot 10^5$	36
4.4	Mean pressure on suction surface, $y/c=0.1$. Angle sweep at $10 \frac{m}{s}$, $Re = 5.102 \cdot 10^4$	37
4.5	Mean pressure on suction surface, $y/c=0.1$. Angle sweep at $20 \frac{m}{s}$, $Re = 1.020 \cdot 10^5$	38
4.6	Mean pressure on suction surface, $y/c=0.1$. Angle sweep at $30 \frac{m}{s}$, $Re = 1.531 \cdot 10^5$	38
4.7	Mean pressure on pressure surface, $y/c = 0.1$. Angle sweep at $10 \frac{m}{s}$, $Re = 5.102 \cdot 10^4$	39
4.8	Mean pressure on pressure surface, $y/c = 0.1$. Angle sweep at $20 \frac{m}{s}$, $Re = 1.020 \cdot 10^5$	39
4.9	Mean pressure on pressure surface, $y/c = 0.1$. Angle sweep at $30 \frac{m}{s}$, $Re = 1.531 \cdot 10^5$	40
4.10	Fluctuating power spectra at 0° $10 \frac{m}{s}$, $Re = 0.5102 \cdot 10^5$ - Front . .	41
4.11	Fluctuating power spectra at 5° $10 \frac{m}{s}$, $Re = 0.5102 \cdot 10^5$ - Front . .	42
4.12	Fluctuating power spectra at 10° $10 \frac{m}{s}$, $Re = 0.5102 \cdot 10^5$ - Front .	42
4.13	Fluctuating power spectra at 15° $10 \frac{m}{s}$, $Re = 0.5102 \cdot 10^5$ - Front .	43
4.14	Power spectra as a function of Strouhal number at 15° $10 \frac{m}{s}$, $Re = 0.5102 \cdot 10^5$ - Front. Note the region highlighted is the region that represents the local peaks observed above in figures 4.10 to 4.13. .	43

4.15	C_p vs x/c α sweep at, $Re = 1.531 \cdot 10^5$	44
A.1	Detailed drawing of tip attachment with taps on top surface. All dimensions in mm unless otherwise specified. Drawing not to scale.	50
A.2	Detailed drawing of tip attachment with taps on front surface. All dimensions in mm unless otherwise specified. Drawing not to scale.	51
A.3	Detailed drawing of model base. All dimensions in mm unless otherwise specified. Drawing not to scale.	52
A.4	Exploded view drawing of assembly of front tip attachment with base. Drawing not to scale.	52
C.1	y/c sweep at $20 \frac{m}{s}$, $Re = 1.204 \cdot 10^5$ - Suction Side	56
C.2	y/c sweep at $20 \frac{m}{s}$, $Re = 1.204 \cdot 10^5$ - Pressure Side	56

List of Tables

2.1	Summary of key parameters tested in the above literature on near-field studies.	21
3.1	Front Taps Coordinates	27
3.2	Top Taps Coordinates	28
3.3	Sample Test Matrix	33

Chapter 1

Introduction

The pattern of vortical, turbulent air originating near the tips of airfoils, commonly known as wingtip trailing vortices has been observed since the early days of heavier than air flight. Indeed, their presence is predicted by fundamental aerodynamic theories such as the Kutta-Joukowski and lifting-line theories. Despite this, studies that attempt to gain a detailed insight into the fundamental flow physics that govern the behaviour of such vortices are scant. Having a greater understanding of such phenomena will allow for better predictions of wake turbulence intensity and propagation, airframe noise generation, flap-tip noise generation, and wingtip noise generation. Additionally, given that wingtip trailing vortices have been identified as a significant source of airframe noise, a better understanding of the mechanisms behind their formation will lead to better methods of mitigating the pernicious effects of airframe generated noise.

Chapter 2

Background

A comprehensive literature review was conducted during the development stage of this investigation and has been reproduced below [2]. The following section outlines the key work done within the field of wingtip trailing vortices. A wide variety of investigations have been conducted ranging from theoretical developments, to experimental and numerical investigations.

2.1 Literature Review

Until this point, research into the structure and properties of wingtip trailing vortices can be roughly divided into three broad areas; development of theoretical vortex behaviour models, ‘far-field’ vortex studies, and ‘near-field’ studies, with the bulk of current research being focused on ‘far-field’ studies. It is important to note, that no formal definition of ‘near-field’ and ‘far field’ have been broadly accepted within academia or industry. Within the context of this review, ‘near-field’ will be used to classify studies that look into the initial formation of tip-vortices, as well as their behaviour within approximately two chordlengths.

‘Far field’ will be used to classify studies that look into the flow characteristics of fully developed vortices that extend beyond to beyond two chordlengths downstream. Within each of these broad fields of study, these investigations can be further broken down into two subcategories: experimental investigations of vortex structure and behaviour, and numerical investigations of vortex structure and behaviour.

2.1.1 Background Motivation Literature

In terms of general airframe noise, the review conducted by Spalart [3], provides a very broad overview of the understanding of the structure and effects of airframe generated vortices. This review was primarily motivated by the desire to improve safety and the efficiency of air traffic control procedures. It notes that the powerful, turbulent effects of airframe generated vortices that departing and arriving aircraft are required to maintain a substantial minimum spacing, increasing airline and airport related costs and delays. The relative lack of knowledge of the initial vortex formation ‘rollup’ is noted. General knowledge of far-field vorticity strength and axial velocity are also summarised. This study indicates, that a better understanding of the formation of these vortices, could lead to potential methods of controlling such vortices resulting in drastic time and cost savings.

One of the earlier studies that looked into the noise generated by airframe vortices, was conducted by Fink [4], of the FAA. This study notes, that although most noise emitted from aircraft are generated by the engines, the relatively fast pace of such improvements, such as those relating to high-bypass turbofan technology, means that airframe generated noise will become the dominant source of noise in the near future. This study conducted measurements of airframe generated noise, and related it to regulatory documentation concerning ‘noise standards’ (FAR Part 36). This study looked at general airframe features (wing-sweep angles,

flap deflection, the presence and size of extended landing gear), in relation to overall noise generated. Additionally, it noted a strong relationship between the extension of high-lift devices and airframe noise generated, indicating that flap/slat-tip vortex generation plays a major part in the generation of such noise.

A study by Storms et al. [5]. was one of the first to pursue the issue of flap-tip vortex generation and subsequent noise generation. This investigation was conducted by placing a rectangular airfoil in a closed-circuit wind tunnel. This airfoil model was equipped with a 30% chord flap, and was instrumented with a large number of pressure taps throughout the wing, for the purposes of determining the total coefficient of lift (C_L). A microphone array was used to measure the noise generated near the extended flap tips. Various ‘treatments’ were then added to the flap-tip, and their effects on both noise and aerodynamic performance were evaluated. Flap-tip vortex structure was investigated using smoke-injecting visualisation techniques. By comparing the acoustic output of vortices produced by various flap-tip treatments, clear relationships between the various treatments and the acoustic output were established. Specifically, raked treatments which restricted spanwise flow had an acoustic dampening effect.

Regarding the wingtips themselves, the most extensive study of acoustic output was performed by Brooks, et al [6]. This study clearly states that airfoil ‘self-generated noise’ develops due to the passing of the turbulent boundary layer over the trailing edge of the airfoil, resulting in ‘vortex shedding’. Predictive methods were developed and presented for airfoil ‘self-generated’ noise under specific conditions. This work was extended by a later study conducted by Moreau, et al [7]. Moreau’s study aimed to generate an acoustic and flow visualisation data-set for a flat-tipped version of the airfoils tested by Brooks, et al. Although predictive methods were not developed from this study, the extensive amount of data generated still sheds light onto the effects that tip geometry can have on vortex generation, and related acoustic output.

2.1.2 Theoretical Models

Wingtip trailing vortices have been of interest to aerodynamicists since the earliest days of aerodynamics research. Prandtl's lifting line theory, and its application to the development of the 'horseshoe vortex' model of finite wing lift is the earliest, but by no means the final, example of an attempt to develop a theoretical model of three dimensional lift. One of the more recent successful attempts at developing a theoretical model of vortex behaviour was performed by Crow [8] in 1970. Starting with the kinematic relation between vorticity and velocity in an incompressible fluid:

$$\mathbf{U}_n = \sum_{m=1}^2 \Gamma_m \int \frac{\mathbf{R}_{mn} \times d\mathbf{L}_m}{4\pi |\mathbf{R}_{mn}|^3} \quad (2.1)$$

Crow developed a linear eigenvalue equation:

$$\frac{\partial \mathbf{r}_n}{\partial t} = \sum_{m=1}^2 \frac{\Gamma_m}{4\pi} \times \left\{ \mathbf{e}_y \int_{-\infty}^{\infty} \frac{\left[(z'_m - z_n) - (x'_m - x_n) \left(\frac{\partial z'_m}{\partial x'_m} \right) \right]}{\left[(x'_m - x_n)^2 + (s_m - s_n)^2 \right]^{\frac{3}{2}}} dx'_m \right. \\ \left. \mathbf{e}_z \int_{-\infty}^{\infty} \left(\frac{3(s_m - s_n)^2 (y'_m - y_n)}{\left[(x'_m - x_n)^2 + (s_m - s_n)^2 \right]^{\frac{5}{2}}} - \frac{\left[(y'_m - y_n) - (x'_m - x_n) \left(\frac{\partial y'_m}{\partial x'_m} \right) \right]}{\left[(x'_m - x_n)^2 + (s_m - s_n)^2 \right]^{\frac{3}{2}}} \right) dx'_m \right\} \quad (2.2)$$

which when evaluated, provides a means for predicting the oscillating behaviour of trailing tip vortices. Crow notes that due to the crude nature of both the equation, and experimental data to date, this relationship requires further investigation.

A theoretical model for predicting the axial velocity within the core of the vortex has been developed by Batchelor [9], and is reproduced below:

$$u_x^2 = U^2 + \int_r^\infty \frac{1}{r^2} \frac{\partial C^2}{\partial r} dr - 2\Delta H \quad (2.3)$$

This model allows for the axial velocity within the vortex core to be either above, or below that of the freestream.

2.1.3 Experimental Far-Field Vortex Studies

Although this investigation is not focused on the far-field behaviour of wingtip trailing vortices, studies that have looked into them are nonetheless useful. Not only do they hint at the specifics behind the motivations of this study, but will offer critical insights into the macro level behaviour that are controlled by near-field phenomena.

One of the earlier attempts at experimentally observing the far-field behaviour of wingtip trailing vortices was conducted by Spreiter and Sacks [10] in 1951. The experimental aspect of this study involved a series of simple flow visualisation experiments conducted within a water tank. The experiment involved dragging a triangular wing model vertically through the water tank, with photographs of the water surface being taken with a standard ‘movie camera’. This test was performed at two different angles of attack, 12° and 20°. The images collected from this investigation can be found below in figure 2.1

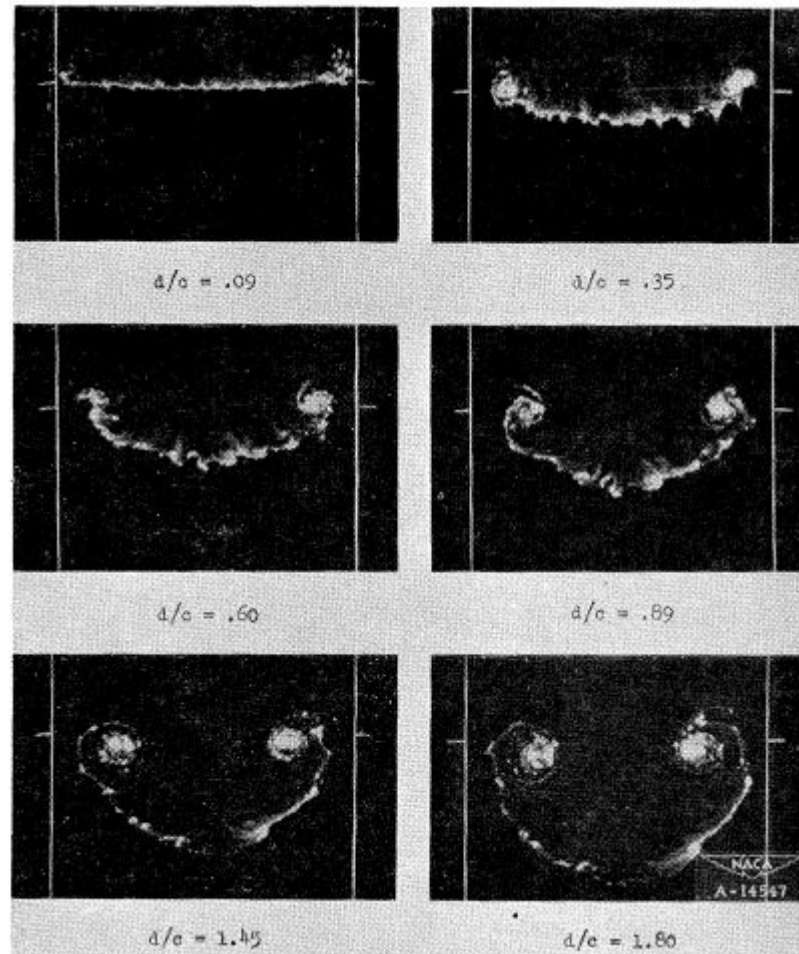


Figure 2.1: Photographs of wake at various stations behind a triangular wing of aspect ratio 2. $\alpha = 12^\circ$, $CL \approx 0.55$.

In 1973, a flight test program directed by Chevalier [11] was conducted in order to study the formation and dissipation of trailing vortices at full scale. Two aircraft were employed in the conduction of the experiment, with smoke ‘grenades’ being mounted on the forward tips of each wing, allowing for visualisation of the vortex flow structure. Data was collected in the form of photographic images, for later analysis. Tests were conducted in both calm and turbulent flight conditions in order to replicate a more complete range of vortex generation situations. This test campaign revealed that a number of different vortex structures were produced. In calm conditions, the vortex structure followed a fluctuating ‘wave’

pattern, and lasted until they later joined up and formed a single ‘vortex ring’ before quickly breaking up. In more turbulent conditions, the vortex fluctuations were more unstable in nature and tended to break up sooner. Figure 2.2 below shows a photographic comparison between the two types of vortex decay. The effects of oscillating control surfaces on vortex structure and breakup were also investigated, resulting in the conclusion that fluctuating the elevator in an oscillatory manner resulted in earlier vortex breakup. Attempts were made to measure the fluctuating decay frequencies, however the scatter of the results rendered this endeavour unfeasible.

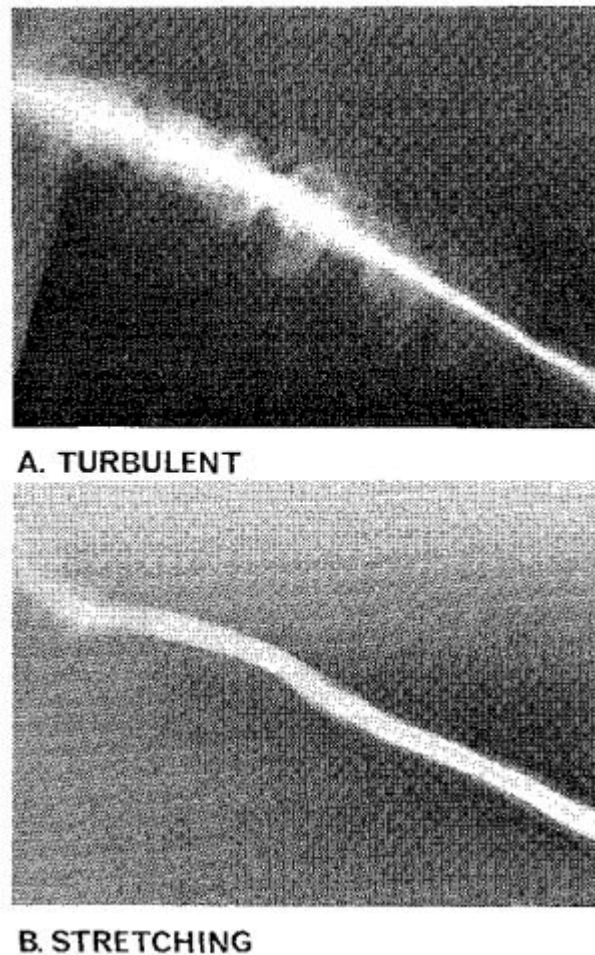


Figure 2.2: Photographs of vortex core dissipation in calm air.

A study conducted by Albano, DeGregoria, and Ragini [12] performed a more

detailed water-tank, towing study of far-field vortex geometries. In particular, this study aimed to conduct a detailed investigation of the type of vortices produced by commercial aircraft. It used a '1:48 scale model of a generic four engine commercial aircraft'. This model was attached to a 'sting' within the tunnel, that allowed for a change in angle of attack. The model had adjustable 'flaps' on each wing, in order to simulate the vortices generated at the flap tips. Although the visual data captured was somewhat poor in quality (see figure 2.3 below), the authors claim that four distinct vortices were observed, two 'primary' vortices associated with the wing tips, and two 'secondary' vortices associated with the flaps.

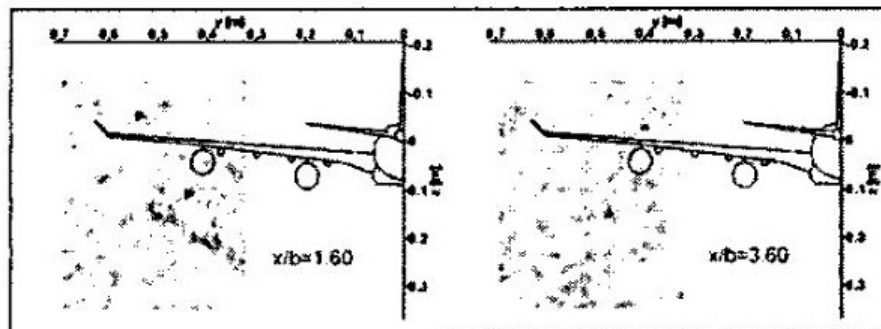


Figure 2.3: Extended near field vortices evolution. The dark shaded regions indicate areas of higher vorticity.

Vortex trajectory and path information were also collected and plotted. A sample of these plots are reproduced in figure 2.4 below. As the authors themselves highlight, this study was very qualitative in nature and further testing is required in order to obtain meaningful data.

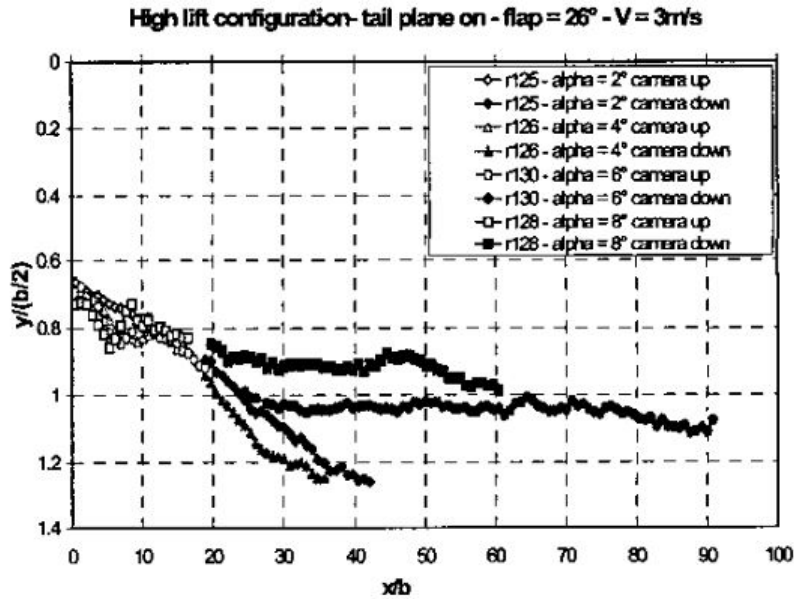


Figure 2.4: Vortex paths varying AoA (y-x plane)

A study performed by R. Stuff [13] examined not only the qualitative structure of far-field vortices, but attempted to gain insights into the ‘breakdown’ of trailing vortices. The study found that trailing vortex breakdown, can be at least partially explained, by instabilities caused when trailing vortices merged. A similar study conducted by Bilanin, Teske, and Williamson [14] attempts to investigate both the breakdown structure of trailing vortices, as well as the viscous transport relations that govern such behaviour.

An ‘integrated’ experimental-numerical study involving a model of a ‘high-agility’ aircraft was conducted by Klar, Breitsamter, Hickel, and Adams [15] in 2011. A 1:15 scale model of a delta-canard configuration aircraft was placed in a 1.8x2.7m test section. This particular test section is noteworthy due to its length $h(21\text{m})$, allowing for investigations of the flow field some 19 ‘spans’ downstream. Investigations were conducted at $Re = 0.5 \cdot 10^6$, and angles of attack of $\alpha = 8^\circ$

and $\alpha = 16^\circ$ were investigated. Non-dimensionalised axial velocity distributions were captured using hot-wire anemometry, and the results are replicated below in figure 2.5.

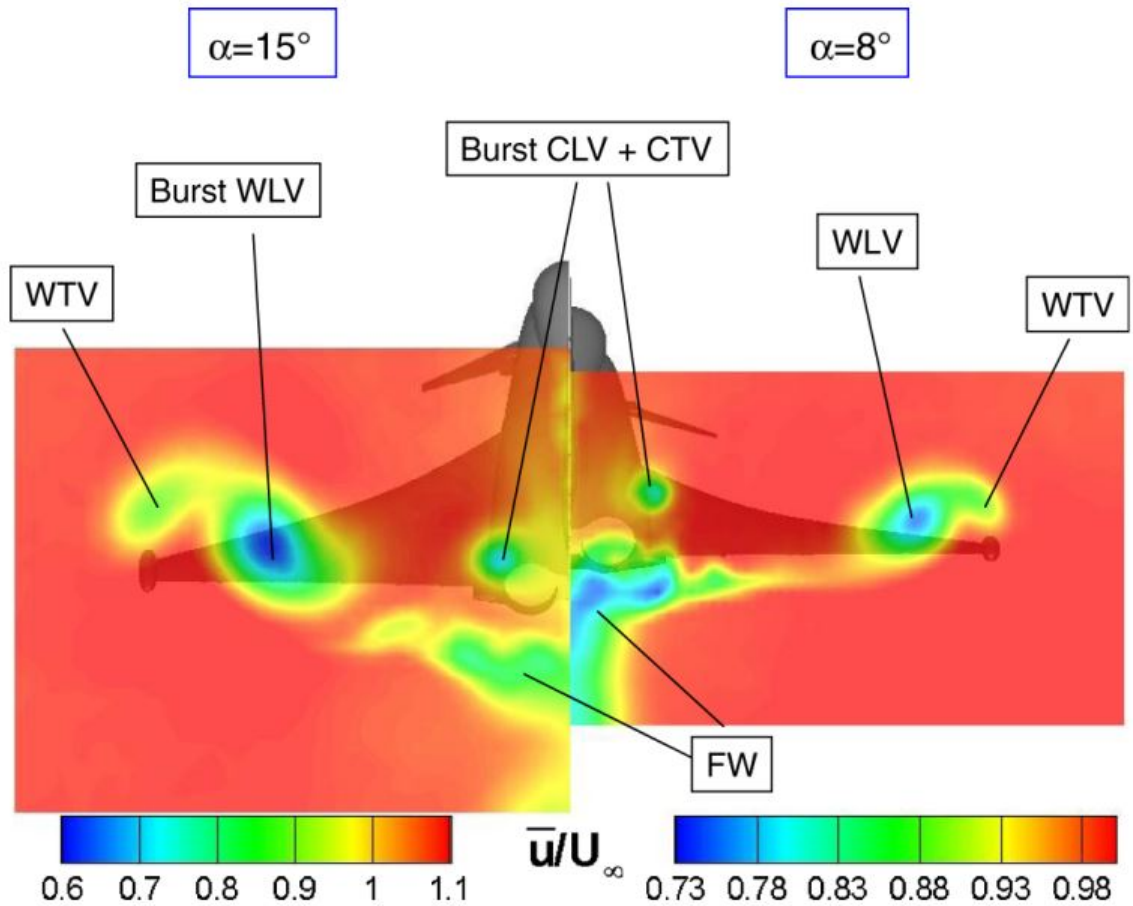


Figure 2.5: Nondimensional axial velocity distributions (\bar{u}/U_∞) at $x/b=0.5$ for $\alpha = 8^\circ$, $\alpha = 15^\circ$. Note, WLW = ‘Wing Leading-Edge Vortex’, WTV = ‘Wing Trailing-Edge Vortex’, CLV = ‘Canard Leading-Edge Vortex’, and CTV = ‘Canard Trailing-Edge Vortex’.

A number of studies have also looked into the far-field axial flow velocity of trailing vortices. One such study conducted by Anderson and Lawton [16] performed a study using a flat tipped model, with a NACA 0015 profile. A rounded ‘cap’ could also be attached to the tip of the model in order to investigate the effect of tip geometry on axial flow parameters. The model was tested in a tunnel

with a 1.2m by 1.2m test section, and a maximum test section velocity of $30 \frac{m}{s}$. Three chord-based Reynold's numbers were investigated, $0.75 \cdot 10^6$, $1 \cdot 10^6$ and $1.25 \cdot 10^6$. As seen below in figure 2.6 below, this investigation demonstrated a relatively linear relationship between a non-dimensionalised vorticity parameter and angle of attack, which is consistent with Pradtl's lifting line theory. A non-dimensionalised velocity parameter was also shown to be linearly proportional to α , and therefore, to the circulation parameter. A study conducted by Zaman, Fagan, and Mankbadi [17] concluded that axial velocity is in fact a more reliable and robust descriptor of axial flow.

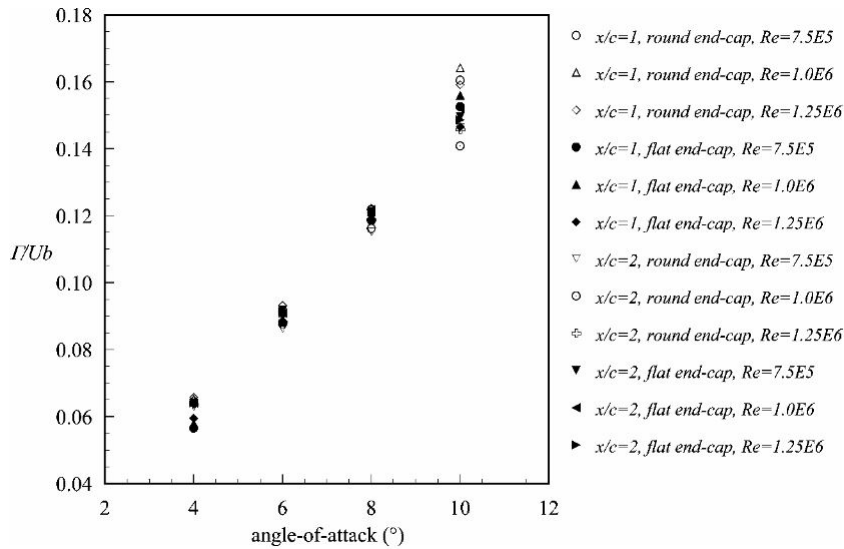


Figure 2.6: Circulation parameter as a function of angle of attack: flat and rounded end-cap data are represented by solid and open symbols, respectively.

Since axial flow velocity was established as a robust descriptor, other studies, such as one conducted by Corsiglia [18]. This study obtained reliable axial flow velocity data of vortices generated by a NACA0015 profile (30.5cm chord), up to thirty span lengths downstream. This particular study managed to experimentally obtain constants for the equations proposed by Nielsen and Schwind [19]. This work was expanded upon by Clifone and Orloff [20], who obtained qualitatively similar data sets for vortices extending some one hundred spans

downstream. This study managed to identify two separate and distinct flow regions in far field vortex behaviour. A study conducted by Iverson [21] used data obtained by studies such as the ones mentioned above in order to develop a ‘vortex velocity scaling parameter’, defined as:

$$\left(\frac{x}{b}\right) \left(\frac{\Gamma_0}{U_\infty b}\right) (AR)^2 f\left(\frac{\Gamma_0}{\nu}\right) \quad (2.4)$$

2.1.4 Computational Far-Field Vortex Studies

One of the earliest computational studies into far-field vortex behaviour was conducted by Hackett and Evans [22] in 1969. This study was motivated by an interest in creating high-lift airfoil geometries. Such geometries would have drastically different trailing vortex profiles, and therefore different stability characteristics. This particular investigation demonstrated that the distance between the centre of rotation of each vortex, and the centre point between the two vortices is described by the following equation:

$$\frac{x_c}{h} = 0.5 \frac{K_2 - K_1}{K_2 + K_1} \quad (2.5)$$

The authors of this study claim that the general effects of new high-lift geometries on lift trends can be reasonably replicated, but were not able to validate their results with experimental data. Although this study, and its results seem to be somewhat crude by today’s standards, it represents an important milestone in terms of computational analysis of vortex related phenomena.

The investigation mentioned earlier, conducted by Klar et al [15], also consisted of a Large Eddy Simulation (LES), CFD investigation of the vortex behaviour of

the aforementioned ‘high-agility’ model. A comparison between the experimental and numerical simulations (see below in figure 2.7 demonstrates the high level of validity of the numerical simulations.

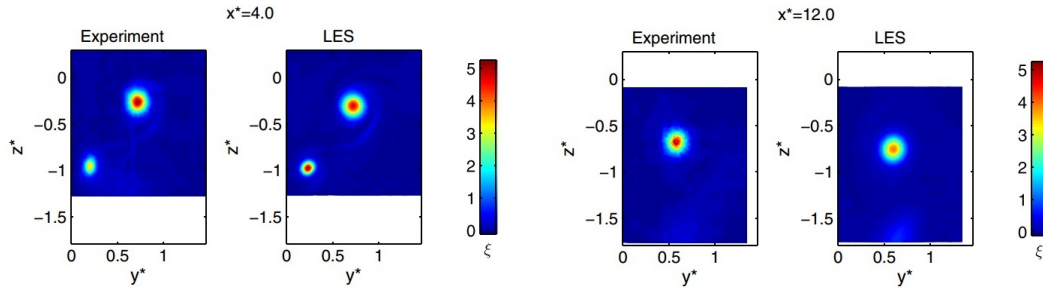


Figure 2.7: Contour plots of nondimensional axial vorticity (denoted here as ξ) at various points downstream of the model.

2.1.5 Experimental Near-Field Vortex Studies

Studies that have focused on the ‘near field’ of vortex formation, have attempted to gain insight into the mechanisms behind vortex formation. Data obtained from these studies (and others like them) will form the basis on which the current investigation will be conducted.

In 1979, Michael Francis and Donald Kennedy [23] conducted an investigation into the flowfield characteristics of a tip vortex during formation. This investigation was conducted using an unswept, rectangular wing with a NACA 64009 profile. The model was tested in a subsonic wind tunnel, at a Reynold’s number of $2.47 \cdot 10^5$, which corresponded with the freestream velocity of thhe upper threshold for the annemometry equipment used. Hot wire annemometry was used to obtain flowfield velocity and vorticity components. It was found that the region near the tip was characterised by high velocity gradients over a very small region. The authors note that the crossflow properties are dependent on all spatial coordinates, and that vortex behaviour likely depends on wingtip geometry. The geometric complexity of the formation of wingtip vortices is clearly demonstrated

by the streamline plots below in figure 2.8.

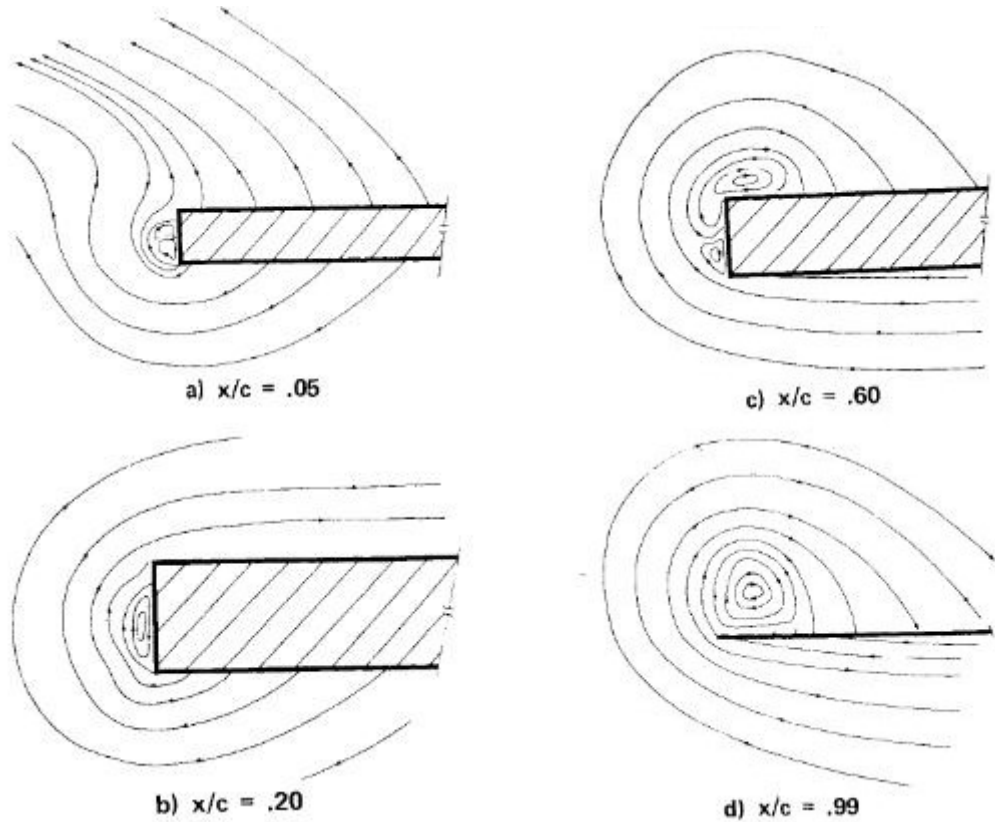


Figure 2.8: Projection of streamlines in the crossflow plane, wing tip region, $\alpha = 4^\circ$, $Re = 2.47 \cdot 10^5$. Of particular note, is the initial formation of the secondary vortex at $x/c = 0.05$.

As can be seen above in figure 2.8, in addition to the primary trailing vortices, the flow near the squared-off tip contains a secondary trailing vortex which forms near the leading edge of the tip. This vortex then grows in such a manner that *"It's growth is restricted to the side portion of the tip until some location (the 60% chord point at $\alpha = 4^\circ$, the condition for maximum lift-to-drag ratio) where it begins to roll over onto the upper surface"*.

Further investigation into the structure and behaviour of tip vortices were performed by Birch and Lee [1] in 2004. The test was conducted in a subsonic wind tunnel, at a Reynolds number of $2.01 \cdot 10^5$, while α ranged from 2° to 18° .

Two rectangular, squared-off sections were used, one with a NACA 0015 profile, and one with a proprietary ‘Bombardier R&D’ cambered profile. The flowfield velocity components were obtained using a seven hole pressure probe. Lift and drag components were obtained using a two-component force balance attached to the model, and mounted below the tunnel apparatus. Vorticity contours were plotted, and are reproduced in figure 2.9. As with the Francis study, the authors here noted the presence of a secondary vortex that formed at the leading edge at the underside of the wing. This secondary vortex wrapped around at approximately $x/c = 0.5$ and joining up with the main vortex, increasing in vorticity as it progressed.

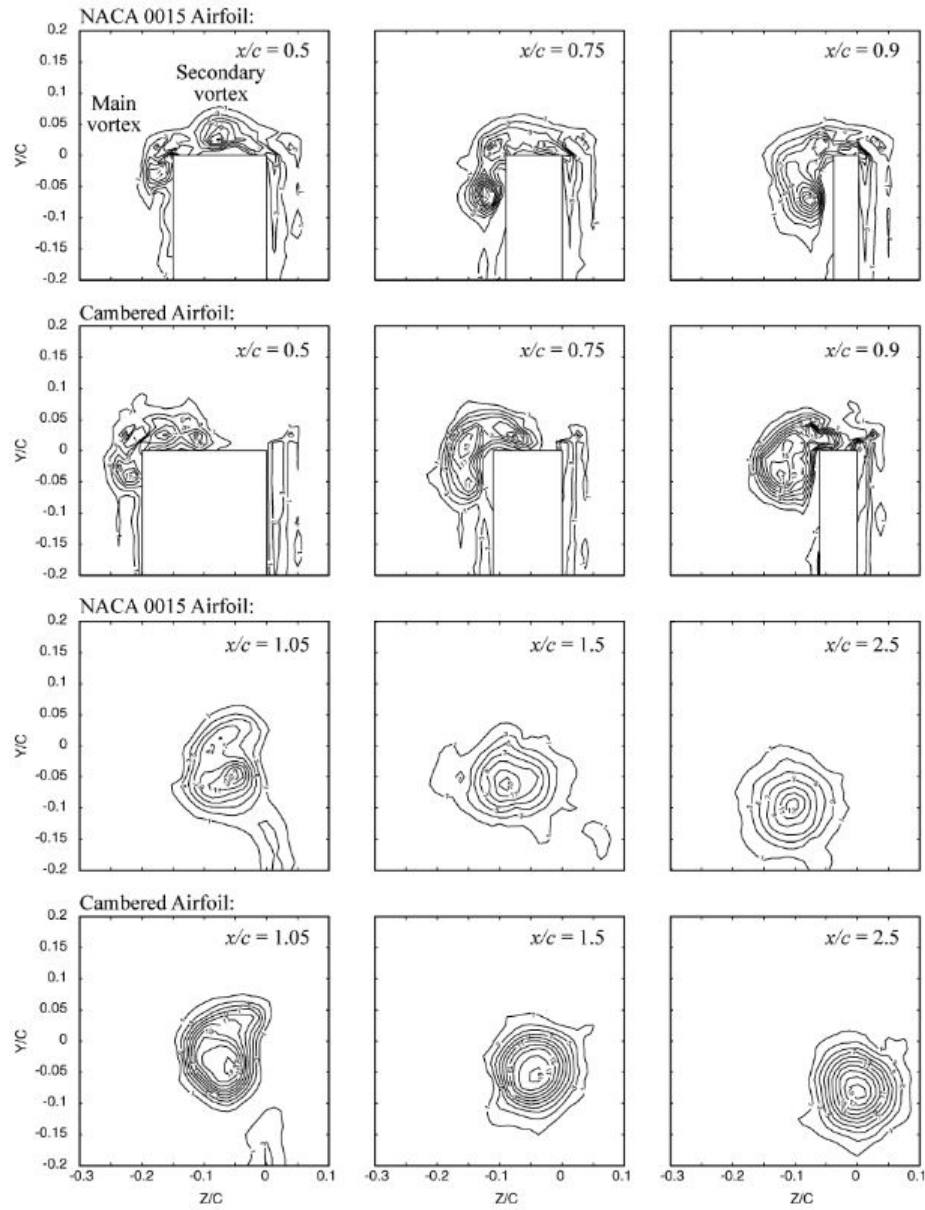


Figure 2.9: Typical normalized vorticity contours for $\alpha = 10^\circ$. [1]

When comparing the symmetric profile with the cambered profile, the authors noted that the secondary vortices produced by the cambered profile were more axisymmetric, tightly wound, and had higher vorticity levels. It was also noted that the axial velocity with the vortex core was highly variable, dipping below, as well as exceeding U_∞ .

A follow up study was conducted by Lee and Pereira [24] in 2010, which compared the near-field behaviour of tip vortices produced by a squared-off airfoil, and a ‘rounded’ airfoil. The authors of this study note that the secondary vortices produced by the rounded tip, when compared with those produced by the squared off tip, were more ‘tightly wound’, and had higher axial flow velocities. Figure 2.10 below contains an illustration of near-field vortex flow visualisation.

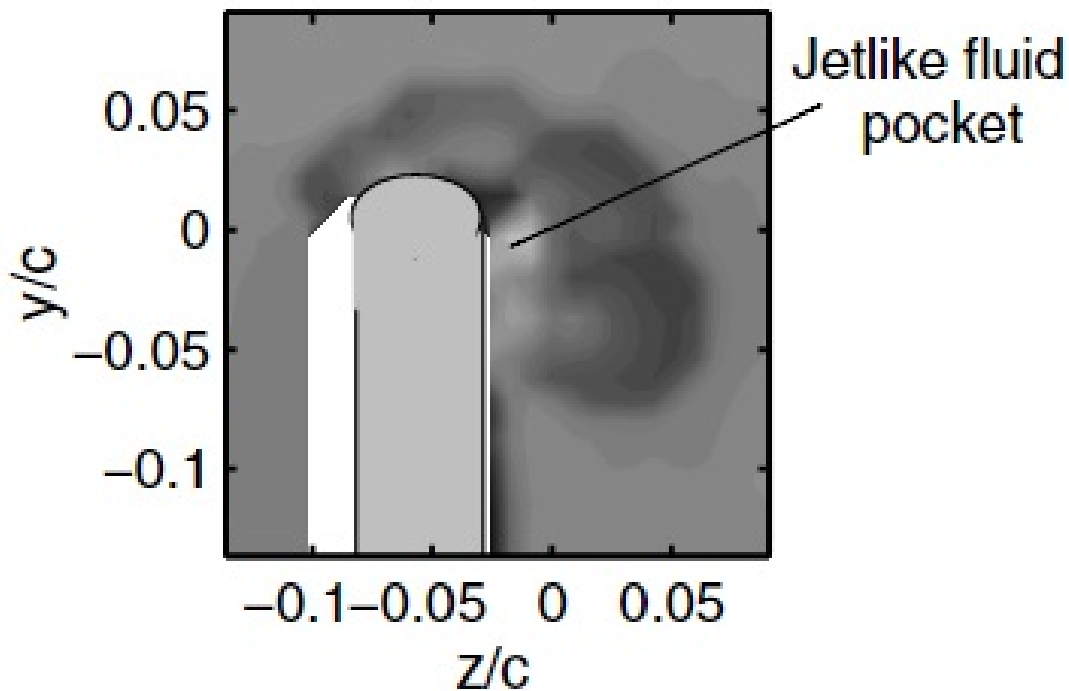


Figure 2.10: An example of a normalised velocity contour plot presented in the study. $x/c=0.8$.

It was noted that downstream axial flow velocity of the tip vortices increased at higher angles of attack. It is hypothesised that this is due shear layers protecting them from the disruptive effects of the trailing edge wake. Qualitatively similar studies have been conducted by Chow, Zilliac, and Bradshaw [25], this time investigating a NACA 0012 profile model with a rounded tip at $Re = 1.6 \cdot 10^6$, at an angle of attack of 10° . Similar trends to those found in the Francis, Birch and Lee studies were found between axial velocity vs angle of attack.

A related study was conducted by Giuini [26] in which flow visualisations of squared and rounded off tips were conducted. Both smoke visualisation (at $Re=3000$) and PIV ($Re = 7.4 \cdot 10^5$) techniques were used in order to provide a comprehensive visual representation of tip vortices. The smoke visualisation images (see figure 2.11 below) allowed for an extremely detailed visual representation of tip vortices.

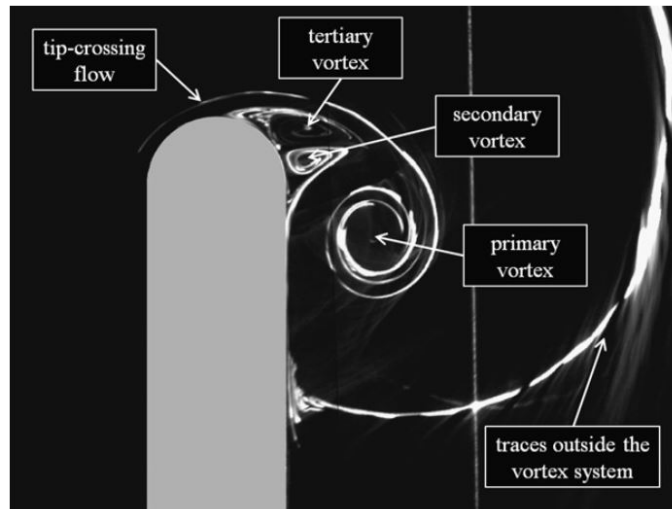


Figure 2.11: Vortex at $Re=3000$, $\alpha = 12^\circ$ on rounded tip; wing section in gray.

The PIV results allowed for the representation of key flow parameters of trailing tip flows; namely vorticity and axial velocity (see figure 2.12).

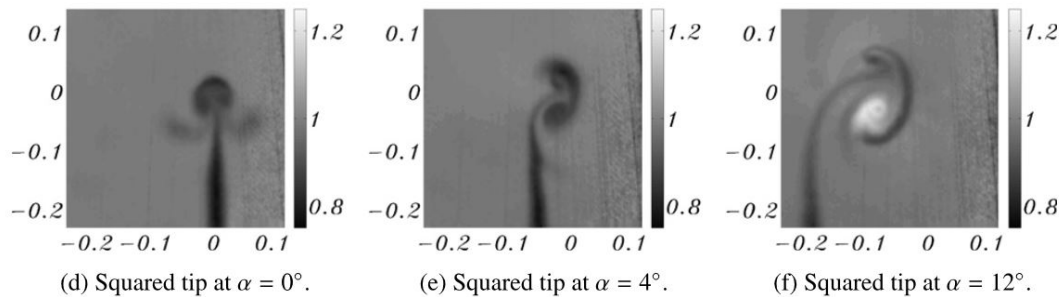


Figure 2.12: Axial velocity at $Re=7.4 \cdot 10^5$, $\alpha = 12^\circ$.

Like the previous studies cited above, the authors of this study noted that fewer vortices were produced by the rounded tips, and those that were produced had higher axial velocities and vorticities. The square tipped airfoils produce more intense secondary vortices, at both the leading and trailing edges. These vortices are highly unsteady, and disturb the primary vortex, contributing to the overall unsteadiness of the flow field. The authors also made an effort to point out that freestream conditions have an outsized impact on the axial component of the tip vortices.

Although work in this particular field is limited, and slightly beyond the scope of the current investigation, it is worth pointing out work done into near-field vortex studies pertaining to rotating airfoils, as per helicopter blade dynamics. A study conducted by Ramasamy, Johnson, and Leishman [27] used Particle-Imaging Velocimetry (PIV) and Laser Doppler Velocimetry (LDV) were used to capture key flow information of rotating airfoils. Unlike conventional airfoil studies, distance from the airfoil trailing edge is defined in terms of ‘wake age’ in degrees. An example of an image produced by LDV is presented in figure 2.13.

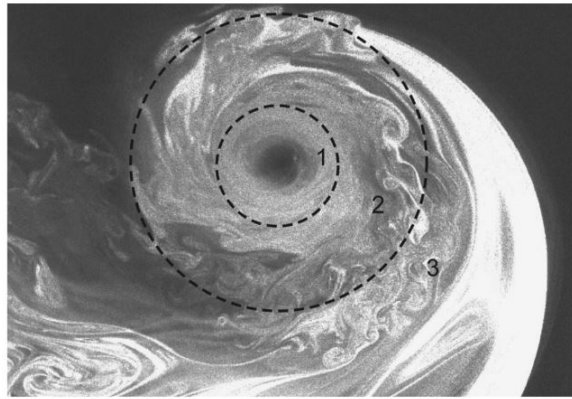


Figure 2.13: Laser light sheet flow visualization of a fully developed blade tip vortex where ‘1’ shows the inner zone free of large turbulent eddies, ‘2’ shows a transitional region with eddies of different scales, and ‘3’ shows an outer, essentially potential flow region.

Extensive flow-field information was collected, including ‘peak swirl’ velocity, vorticity, and core size. Additionally, significant correlation was found between both measurement techniques.

Summary of Near-Field Experimental Studies

Table 2.1: Summary of key parameters tested in the above literature on near-field studies.

Study	Profile	$\alpha(^{\circ})$	c (m)	Re
Francis	NACA 64009	4	18.3	$2.47 \cdot 10^5$
Birch	NACA 0015, ‘cambered’ airfoil	2-18, emphasis on 10	0.254	$2.01 \cdot 10^5$
Lee	NACA0012, square and rounded	4,5,6,9,10,11,15	0.280	$3.07 \cdot 10^5$
Guini	NACA0012, square and rounded	0,4,12	0.76	$3.0 \cdot 10^3, 7.4 \cdot 10^5$

The majority of surface pressure measurements, such as the ones conducted during studies by Storms [5], Walker [28], McDevitt [29] have primarily focused on experimentally obtaining the coefficient of pressure, and other aerodynamic coefficients derived from it. Few if any of these measurements are directly related to trailing vortex formation, and none are of especially high fidelity, especially in the spanwise direction, or towards the airfoil tip.

2.1.6 Numerical Near-Field Vortex Studies and Surface Pressure Measurements

In 1995, a study performed by Kandil, Wong, Adam, and Liu [30], conducted a numerical investigation, comparing how a number of different turbulence models modeled the near field behaviour of tip-vortex flows. The software used employed the Reynolds Averaged Navier-Stokes equations, along with the turbulence models of Baldwin and Lomax, Spalart and Allmaras, and the ‘two-equation shear stress transport’ model of Menter. The study found that the Baldwin and Lomax, as well as the Spalart-Allmaras models, provided superior modelling of tip vortex phenomena when compared with the two equation shear stress transport formulation.

2.1.7 Summary

The majority of research into wingtip trailing vortices focus on far-field behaviour, specifically, geometric structure and mean flow parameter determination. A number of near field studies have also been performed that look into the visual features of vortex formation and development. Numerical studies have also been conducted into both far field and near field flows. To date, most, if not all, airfoil surface pressure measurements have been conducted in order to experimentally determine the coefficient of pressure and associated parameters. The lack of high fidelity surface pressure measurements near the airfoil tip represents a significant gap in experimental knowledge, and therefore an area of opportunity for further research work.

Chapter 3

Aims and Methodology

3.1 Aims

The primary aim of this investigation is to gain a better understanding of the flow physics underpinning the formation of wingtip vortex generation.[2] This will be done by obtaining both mean and fluctuating surface pressure measurements around the tip region of a squared-off symmetric airfoil over a variety of α and Re values. The data obtained in this study provides insights into vortex formation and can serve as a source of validation for CFD investigations. The fluctuating surface pressure data can also serve as a direct means of studying noise generated by the formation of tip vortices.

3.2 Methodology

3.2.1 Facilities

The tests that have been conducted in this investigation were performed in a benchtop, subsonic wind tunnel with a working test section of 125x125mm, and a maximum test section velocity of $35 \frac{m}{s}$. Figure 3.1 below shows the fully assembled wind tunnel to be used.

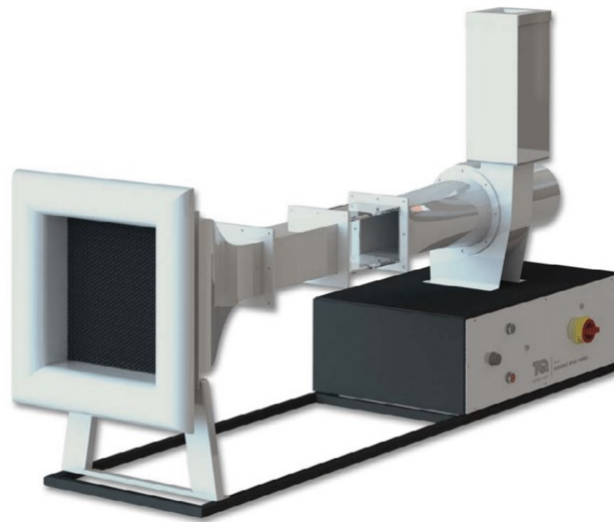


Figure 3.1: Benchtop wind tunnel model AF1125, manufactured by TECQUOPMENT.

3.2.2 Test Geometry

The coordinate system that is used throughout this work is detailed below in figure 3.2. Note that the origin is at the leading edge of the airfoil tip (penetrating furthest into the freestream).

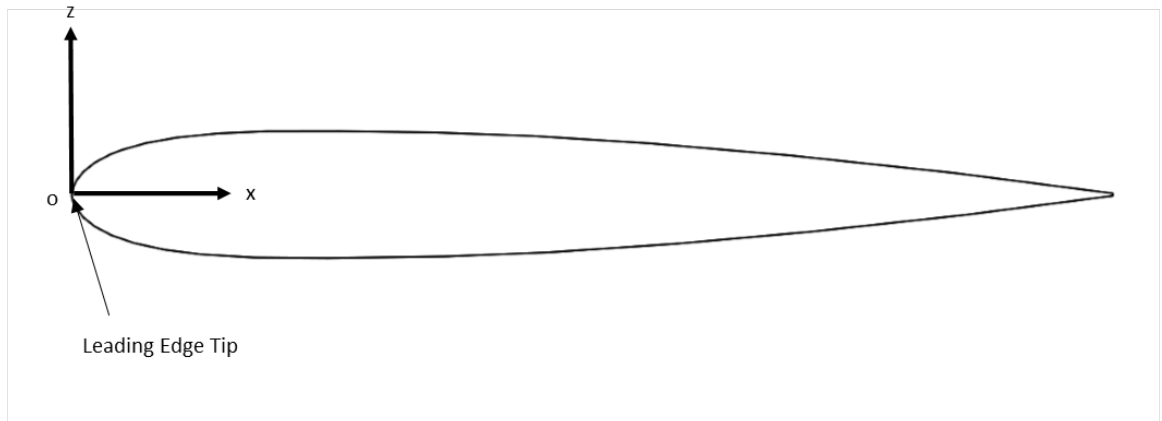


Figure 3.2: Coordinate definition, x-z

The airfoil test model consists of three components, a ‘base’ mounting section, a ‘tip-taps’ section, and a ‘top-surface-taps’ section. The base section is to be attached to the test section wall. This base section will be hollowed out, in order to allow for tubing to run between the ‘tapped’ components, and the pressure transducers, see figure 3.3 below for details.

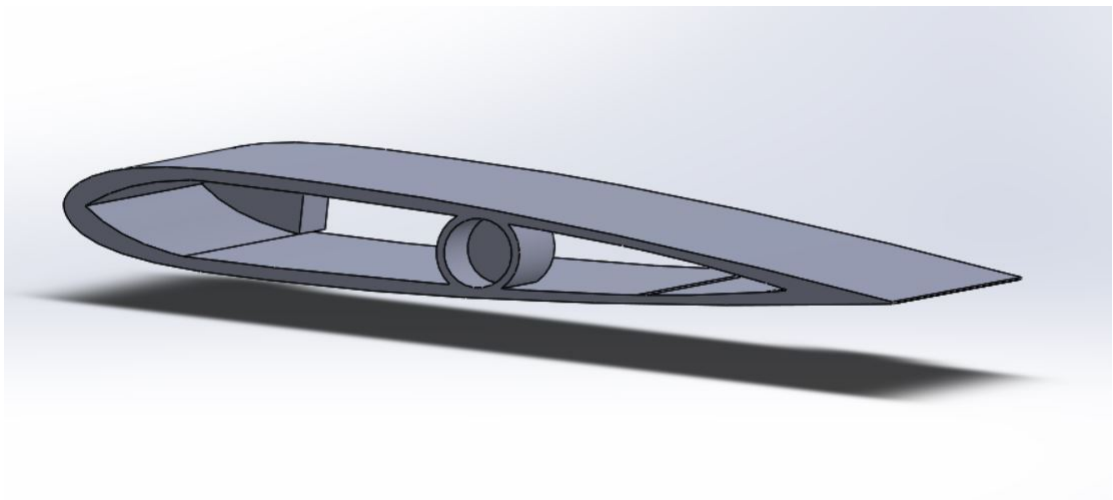


Figure 3.3: Model mount component, to be screwed into the tunnel wall.

Two separate airfoil sections will be attached to this ‘base’. One which will contain pressure taps along the tip surface (figure 3.4), and one which will contain

pressure taps along the top of the tip surface (figure 3.5), both of which will have a ‘squared-off’ profile. All three components have a NACA 0012 profile, with a 80mm chord. The fully assembled components have an aspect ratio of 1. The ‘Front-Tapped’ attachment contains a total of 23 pressure taps, each being 0.8mm in diameter. The ‘Top-Tapped’ attachment contains a total of 25 taps, also having a diameter of 0.8mm.

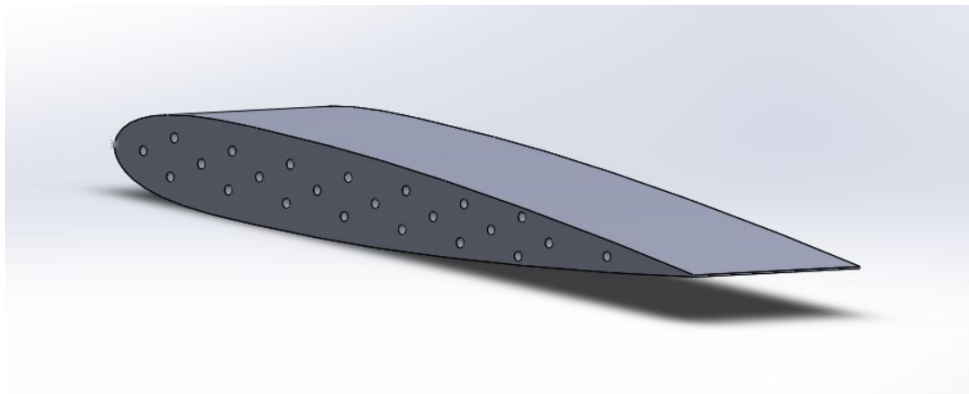


Figure 3.4: ‘Front-Tapped’ attachment.

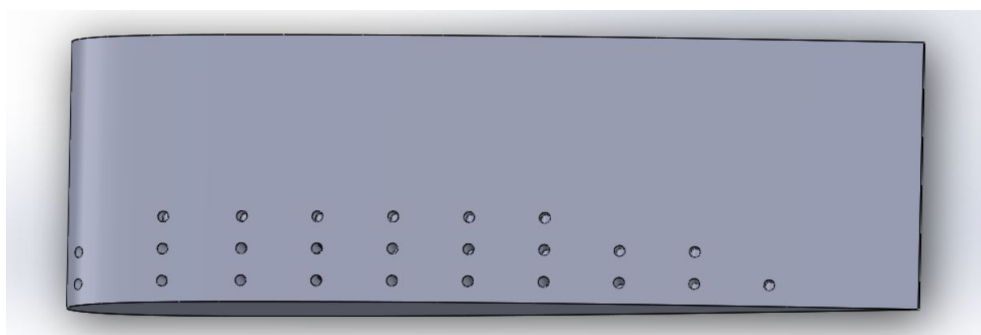


Figure 3.5: ‘Top-Tapped’ attachment.

The coordinates of the taps are given below in tables 3.1 and

Table 3.1: Front Taps Coordinates

Tap Number	x (mm)	y(mm)	z(mm)
1	4	0	0
2	8	0	2
3	8	0	-2
4	12	0	0
5	16	0	2
6	16	0	-2
7	20	0	0
8	24	0	2
9	24	0	-2
10	28	0	0
11	32	0	2
12	32	0	-2
13	36	0	0
14	40	0	2
15	40	0	-2
16	44	0	0
17	48	0	2
18	48	0	-2
19	52	0	0
20	56	0	2
21	56	0	-2
22	60	0	0
23	68	0	0

Table 3.2: Top Taps Coordinates

Tap	x	y	z
1	1.32	2	2.13
2	1.32	5	2.13
3	9.54	2	4.55
4	9.54	5	4.55
5	9.54	8	4.55
6	16.98	2	4.88
7	16.98	5	4.88
8	16.98	8	4.88
9	24.07	2	4.8
10	24.07	5	4.8
11	24.07	8	4.8
12	31.16	2	4.67
13	31.16	5	4.67
14	31.16	8	4.67
15	38.25	2	4.34
16	38.25	5	4.34
17	38.25	8	4.34
18	45.29	2	3.86
19	45.29	5	3.86
20	45.29	8	3.86
21	52.3	2	3.28
22	52.3	5	3.28
23	59.27	2	2.6
24	59.27	5	2.6
25	66.21	2	1.85

The manner in which the base, tip, and tubing fit together is illustrated below in figures 3.6 and 3.7

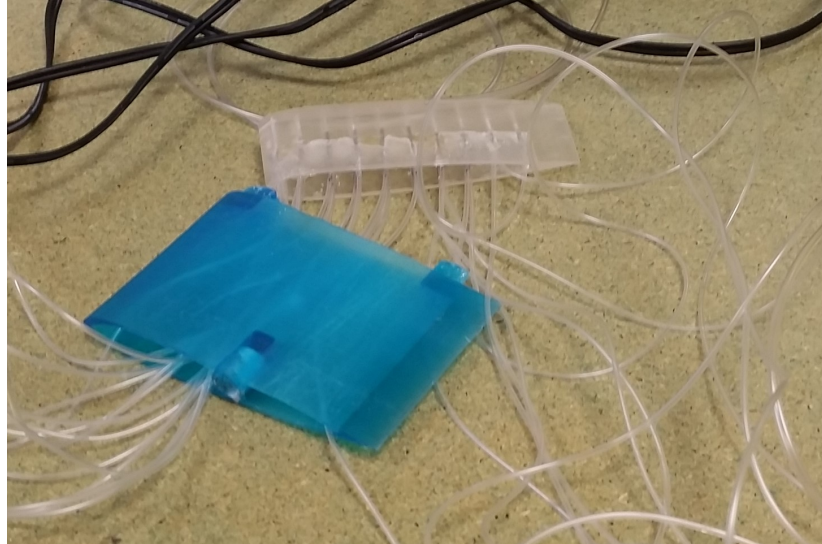


Figure 3.6: Example of assembly: This is an image of the 'front' taps attachment being attached to the 'base'.

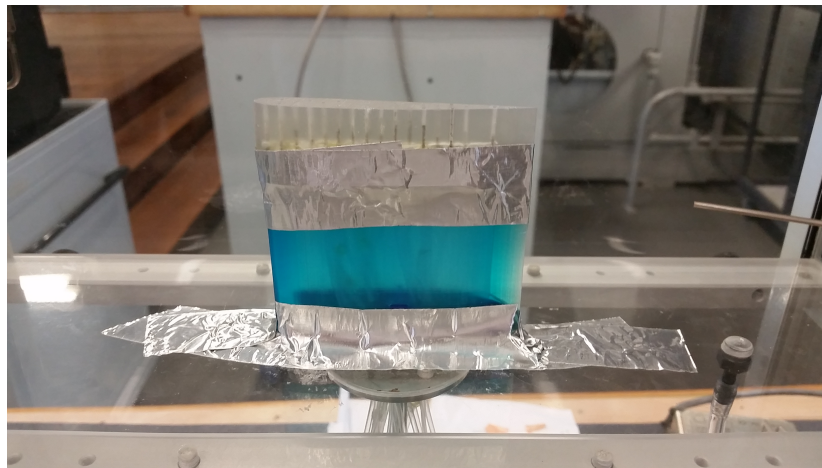


Figure 3.7: The 'front' taps and 'base' fully assembled and installed within the wind tunnel. Note that the 'top' and 'base' have been secured together using speed tape, and the whole assembly has been secured to the test section 'floor' using speed tape.

Detailed drawings of the base, attachments and assembly are given in appendix A.

The number of flow conditions that were tested were dependent on facility availability. The first tests that were conducted were at the highest Reynolds number that the wind tunnel can produce. At this freestream velocity (approximately 35 m/s), an angle of attack sweep from 0° to 20° was conducted. Both mean and fluctuating pressure data were taken for each angle of attack.

Assembly Placement in Test-Section

The model assembly was mounted on the bottom side of the interior of the test section. The model was mounted by at it's centre, to the centre of the bottom of the test section. See figure 3.8 for illustration. Plastic tubing was channelled through a hole in the bottom of the test section in order to connect them to the required data acquisition equipment. See sections related to mean and unsteady pressure measurements for further details on the connections between the model and the data acquisition equipment.

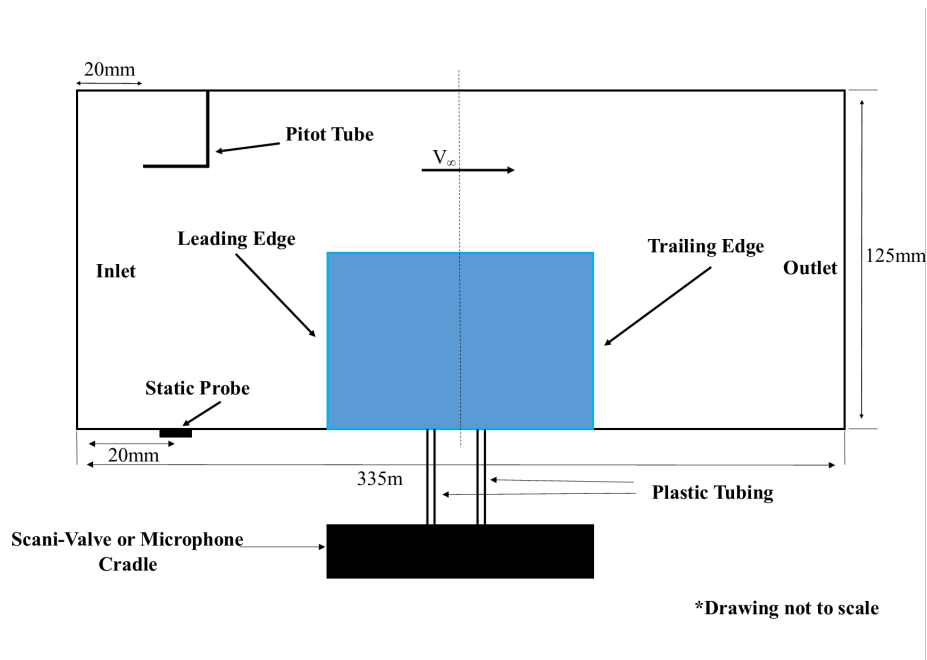


Figure 3.8: Diagram illustrating the placement of the model assembly within the tunnel test section.

Mean Pressure Measurements

The mean pressure values were acquired using a scanivalve unit. This was conducted four times, twice for each attachment. A compressed test matrix is given below in Table (3.3). Given that mean and fluctuating pressure have been acquired separately, each piece of equipment was set up in advanced in order to efficiently collect the data. The scanivalve used to acquire mean pressure data contains contains 16 channels, two of which are reserved for q_∞/V_∞ measurements, in a single unit. This means that the data collection for each test condition has to be conducted in two runs in order to capture all of the data points. 0.83mm outer diameter hypodermic needles will have to be installed within each test model, connected to 0.83mm inner diameter tubing. These tubes are connected to 1.6mm inner diameter tubes by simply fitting the smaller tubes within the larger tubes and using a sealant in order to ensure an air-tight fit.

Fluctuating Pressure Measurement

Fluctuating pressure was acquired with a series of 7mm, 40PH CCP Free-Field Array G.R.A.S. microphones. A series of 8 such microphones are arranged such that 8 of them are able to be hooked up to 0.8mm inner diameter tubing. This will allow for the fluctuating pressure to be measured using the ‘remote microphone’ method. Microphone data was gathered and processed using a National Instruments PXI data acquisition system [31]. Data acquisition scripts have been drafted in order to process the data from each set of tests using MATLAB. A copy of this script can be found in Appendix B. Experimental validation of this general procedure is outlined by England and Richards [32].

Once the pressure data was collected, it was processed, with appropriate fluctuating pressure spectra plotted and mean pressure contours mapped. Correlations

were drawn between the mean pressure contours generated by the data gathered here and the vortex formation behaviour observed in the literature.

Microphone Calibration Procedure:

Given that the microphones are calibrated for use as stand-alone free field microphones, the microphones had to be re-calibrated in order to be used in conjunction with the cradle/model setup. The signals generated by the speaker, reference microphone, and microphone attached to the pressure tap in question are compared in order to develop an appropriate transfer function which is used in place of the given sensitivity of the microphone. The procedure used to calibrate the microphones is fully outlined by Awasthi [33].

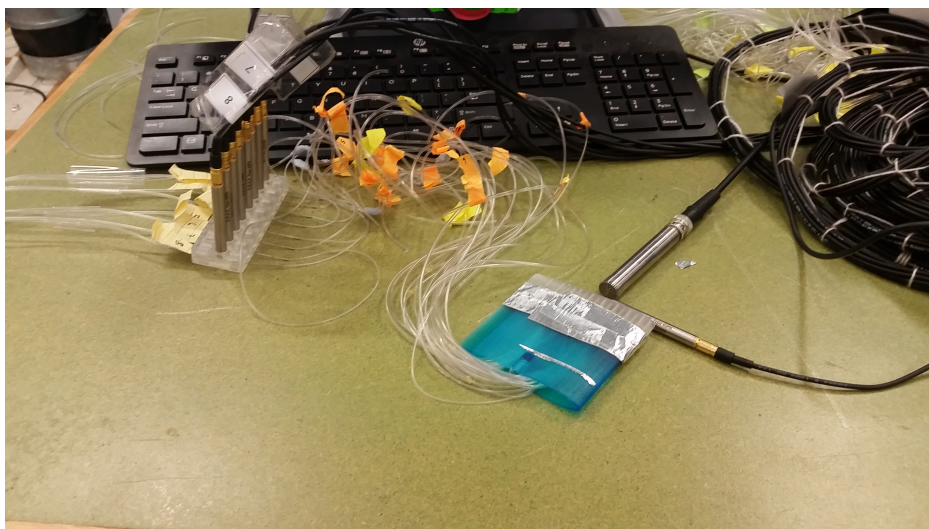


Figure 3.9: Broader view of calibration setup. Note the cradle in which the microphones sit (used during measurement as well as calibration) and the connection between the cradle outputs and the model taps.



Figure 3.10: Close up, birds-eye view of the calibration setup. Note the perpendicular positioning of the a)reference speaker, b)reference microphone, and the model taps.

3.2.3 Test Matrix

Table 3.3: Sample Test Matrix

Attachment	Re	Associated U_∞ (m/s)	α ($^\circ$)
Front, Top	$0.25 - 1.5 \cdot 10^5$	5-35	0-20

Chapter 4

Results and Discussion

4.1 Results

4.1.1 Mean Pressure Measurements

When examining the following data, it is worth noting that the data taken for angles 0° and 10° , and 5° and 15° were taken on separate days. In terms of the mean pressure measurements taken at the tip, very little is known about the flow physics within the region being investigated. The data here must therefore be evaluated mostly as it stands. Examining Figures 4.1 to 4.3 a common general pattern throughout all angles and Re emerges. Pressure begins at a relatively low point, sharply drops at approximately $x/c = 0.2$, sharply drops again, and then slowly increases again. In terms of the first pressure peak, the most noticeable parameter that affects the magnitude of the peak seems to be angle of attack, with the peak decreasing in magnitude along with angle of attack. The main effect of increasing Re appears to be an increase in magnitude in the pressure drop that occurs following the initial peak. As per classical aerodynamics theory, pressure peaks are associated with slower fluid flow and/or flow detachment, whereas pressure decreases are associated with faster fluid flow and/or reattachment. How-

ever, it is worth noting that the above stated relationship between pressure and detachment/reattachment points are based on an assumption of laminar flow. As the flow around the tip region is highly turbulent, this assumption no longer holds true, and therefore, conclusions regarding attachment/reattachment points can only ever be at least somewhat suspect. It is interesting to note that the regions associated with the sudden pressure peaks and troughs are associated with the region of the tip in which the primary and secondary vortices ‘roll up’ (moves from the pressure surface to the suction surface), as per the work done by Francis [23] and Birch [1]. Absent other high resolution data-sets, direct relationships between vortex formation and characteristics can’t be drawn. The data gathered here can however be used as a starting point for high resolution particle imaging velocimetry (PIV), smoke visualisation, and hot-wire anemometry investigations.

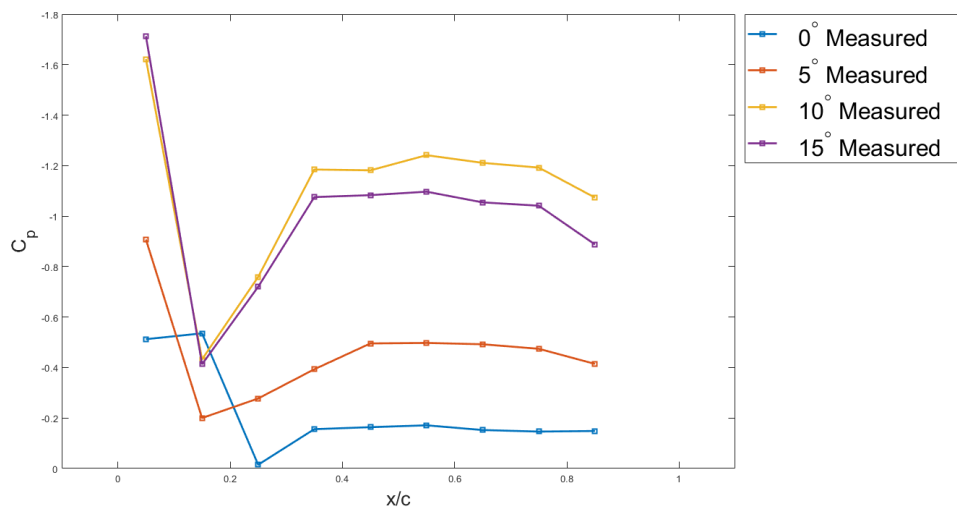


Figure 4.1: Mean pressure on ‘front’ surface. Angle sweep at $10^{\frac{m}{s}}$, $Re = 5.102 \cdot 10^4$

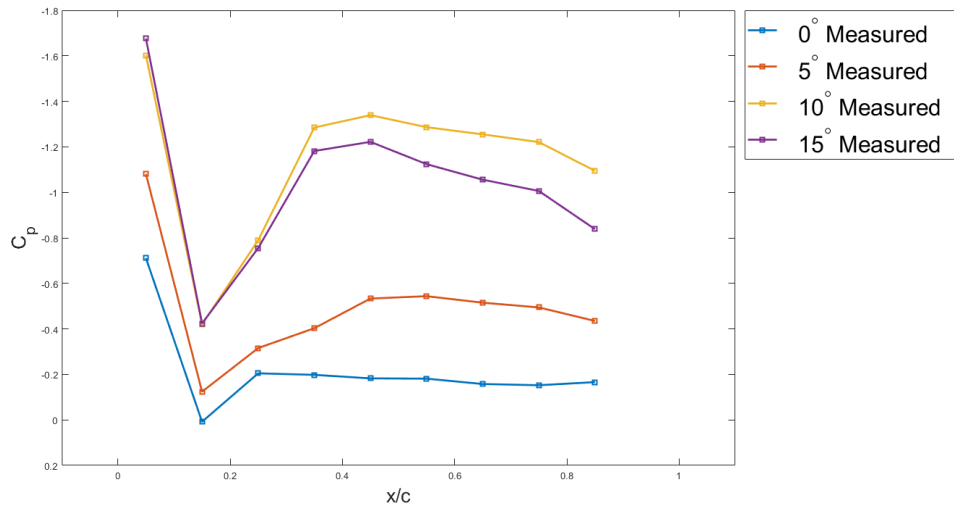


Figure 4.2: Mean pressure on ‘front’ surface. Angle sweep at $20 \frac{m}{s}$, $Re = 1.020 \cdot 10^5$

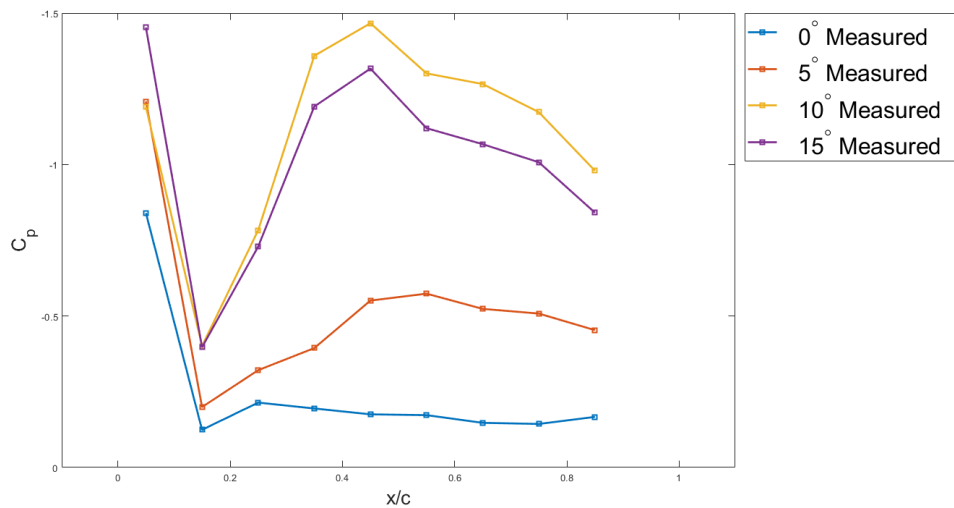


Figure 4.3: Mean pressure on ‘front’ surface. Angle sweep at $30 \frac{m}{s}$, $Re = 1.531 \cdot 10^5$

The following results are the pressure distribution data for the top/suction portion of the airfoil. The results presented here are from data taken furthest inboard from the tip. Measured results are compared with theoretical 2D values, as taken from xfoil software. It is important to note that the ‘viscous model’ was turned on when extracting the theoretical data from xfoil [34]. Regarding pressure measurements taken at the suction and pressure sides of the airfoil tip, it is worth comparing

the data gathered during this investigation with classical, 2D aerodynamic theory. This comparison allows for direct insights into how 3D effects impact mean surface pressure around the tip. The theoretical values for 2D C_p vs x/c data have been taken from the ‘xfoil’ software suite. This piece of software combines traditional vortex panel methods and a fully-coupled viscous/inviscid interaction method [35]. Regarding the suction side cases (see figures 4.4 to 4.6), in the 10 m/s case, a significant pressure spike occurs at $x/c = 0.3$. From that point onward, there does not seem to be any coherent pattern to the C_p distribution. At 0° and 15° , there seems to be a slight pressure recovery (at different rates), while at 5° and 10° , C_p continues to drop (again, at different rates). In the 20 m/s and 30 m/s suction side cases, a distinct pressure spike occurs at $x/c = 0.3$, which is followed by a sudden but less dramatic recovery. From $x/c = 0.4$ and onward, there is a continued recovery at 0° and 5° angles of attack, while slow pressure drops are observed at 10° and 15° angles of attack.

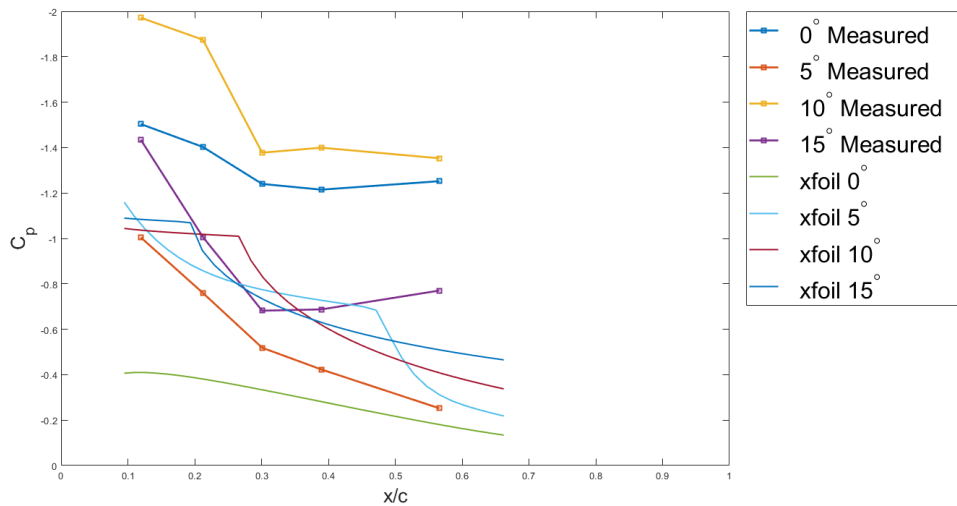


Figure 4.4: Mean pressure on suction surface, $y/c=0.1$. Angle sweep at $10 \frac{m}{s}$, $Re = 5.102 \cdot 10^4$

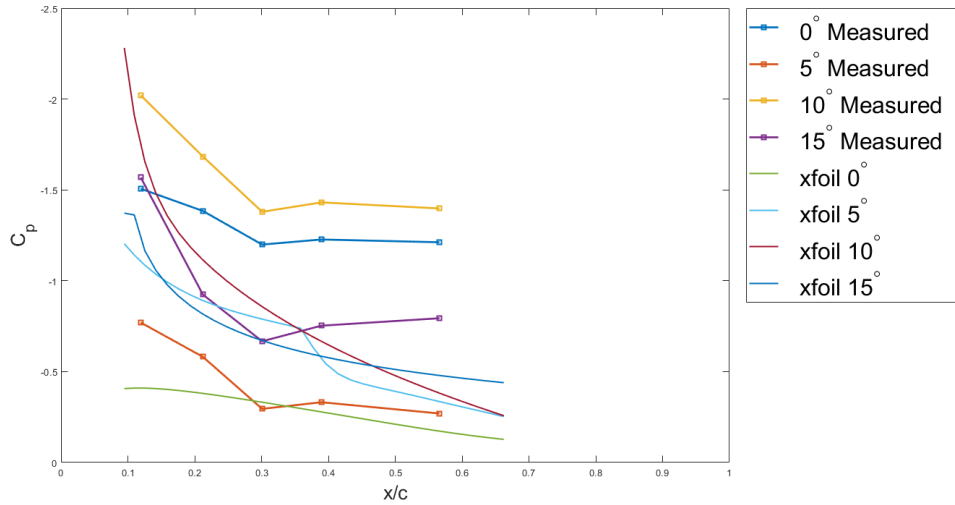


Figure 4.5: Mean pressure on suction surface, $y/c=0.1$. Angle sweep at $20 \frac{m}{s}$, $Re = 1.020 \cdot 10^5$

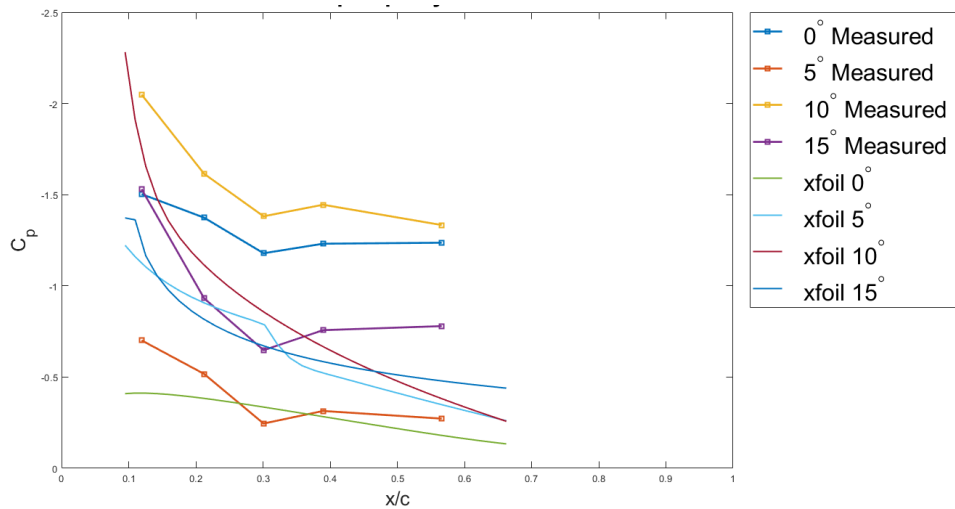


Figure 4.6: Mean pressure on suction surface, $y/c=0.1$. Angle sweep at $30 \frac{m}{s}$, $Re = 1.531 \cdot 10^5$

The following results in figures are the pressure distribution data for the bottom/pressure surface of the airfoil. The results presented here are from data taken furthest inboard from the tip. As with the ‘top’ values, measured results are compared with theoretical 2D values. Regarding the pressure side cases (see figures 4.7 to 4.9), a more discernible pattern seems to emerge. All V_∞ cases seem

to exhibit a pressure spike at $x/c = 0.3$, which is followed by a steady recovery. A slight but notable exception is the 0° , 20 m/s case, in which a very slight drop can be observed at the point following $x/c = 0.4$.

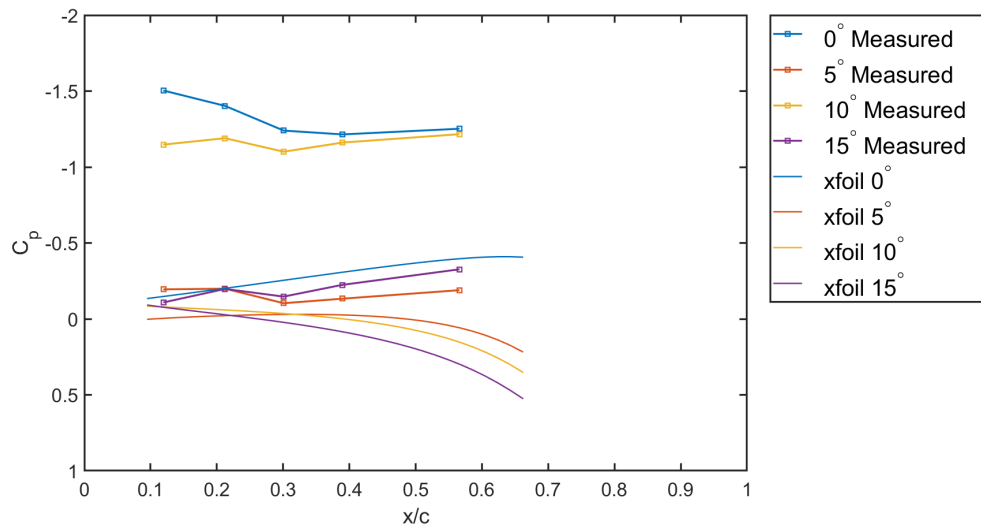


Figure 4.7: Mean pressure on pressure surface, $y/c = 0.1$. Angle sweep at $10 \frac{m}{s}$, $Re = 5.102 \cdot 10^4$

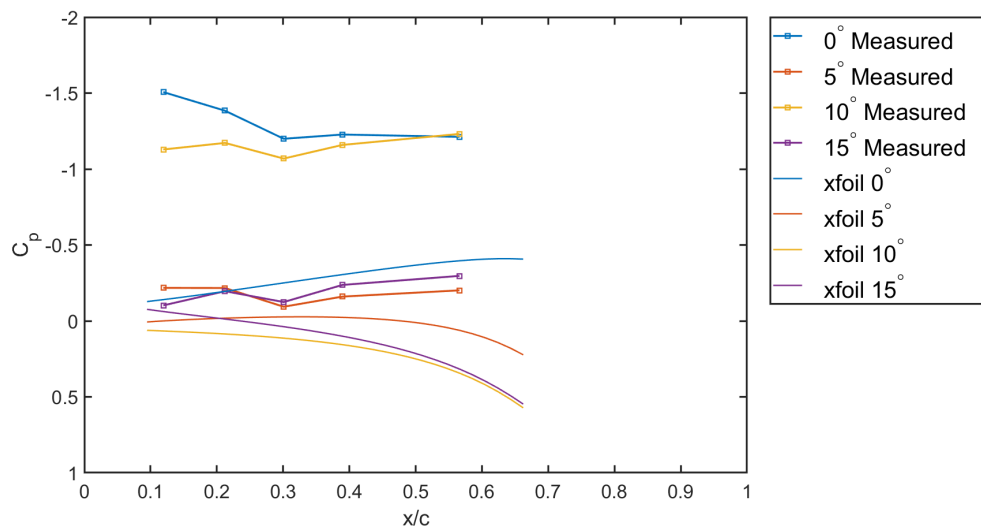


Figure 4.8: Mean pressure on pressure surface, $y/c = 0.1$. Angle sweep at $20 \frac{m}{s}$, $Re = 1.020 \cdot 10^5$

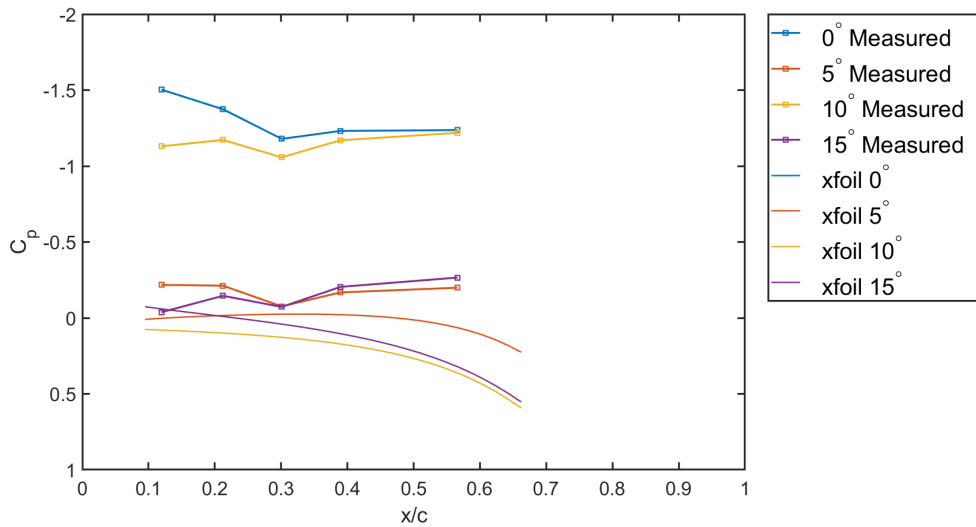


Figure 4.9: Mean pressure on pressure surface, $y/c = 0.1$. Angle sweep at $30 \frac{m}{s}$, $Re = 1.531 \cdot 10^5$

In addition to the fact that the measurements were taken on different days, indicating the possibility of repeatability issues inherent in taking such measurements within this flow region, it is also worth examining the highly irregular nature of the flow near the airfoil tip. While the C_p values fall within an acceptable margin in relation to the theoretical values, the lack of a coherent recovery/fall pattern following the initial pressure spike indicates that the flow within the tip region, even relatively inboard, is highly irregular. This is further supported by the plots presented in Appendix C, in which pressure oscillations between $x/c = 0.2$ and $x/c = 0.5$ are highly volatile. It is very possible that these irregularities are a result of the vortex roll up that has been demonstrated in literature to occur within this region. Unsteady pressure measurements should therefore be examined in order to gain further insights into the nature of the turbulence within this region.

4.1.2 Fluctuating Pressure Results

Fluctuating pressure results along the front of the airfoil are presented below in figures 4.10 to 4.13. Observe the general spike in pressure at a frequency of approximately $5 \cdot 10^3$ Hz at all locations except for 0.35, as well as the consistently low magnitude (close to the ‘zero’ output of the microphone, see appendix B) of the pressure at 0.35. This ‘muffled’ output roughly coincides with the observed ‘roll up’ region, as well as the pressure drop/recovery observed in the front mean pressure results (figures 4.1 to 4.3). The overall magnitude of the pressure fluctuations jumps up when transitioning from 0° to 5° , but no real relationship between fluctuation magnitude and increase in angle of attack beyond 5° . This is noteworthy considering the results presented by Lee et al. [24], in which axial vortex velocity was shown to increase along with angle of attack. This indicates that the relationship between axial flow velocity and vortex fluctuation frequency are not necessarily directly related.

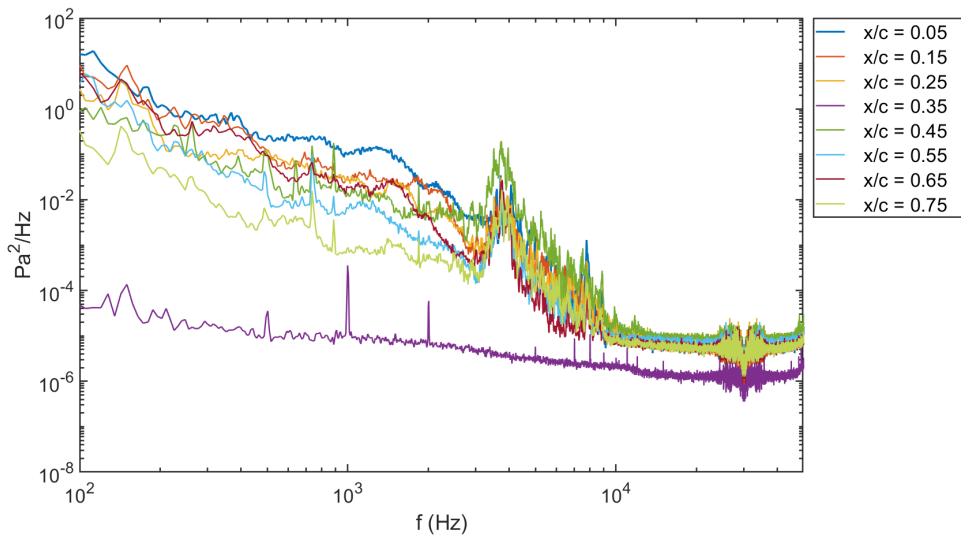


Figure 4.10: Fluctuating power spectra at 0° $10 \frac{m}{s}$, $Re = 0.5102 \cdot 10^5$ - Front

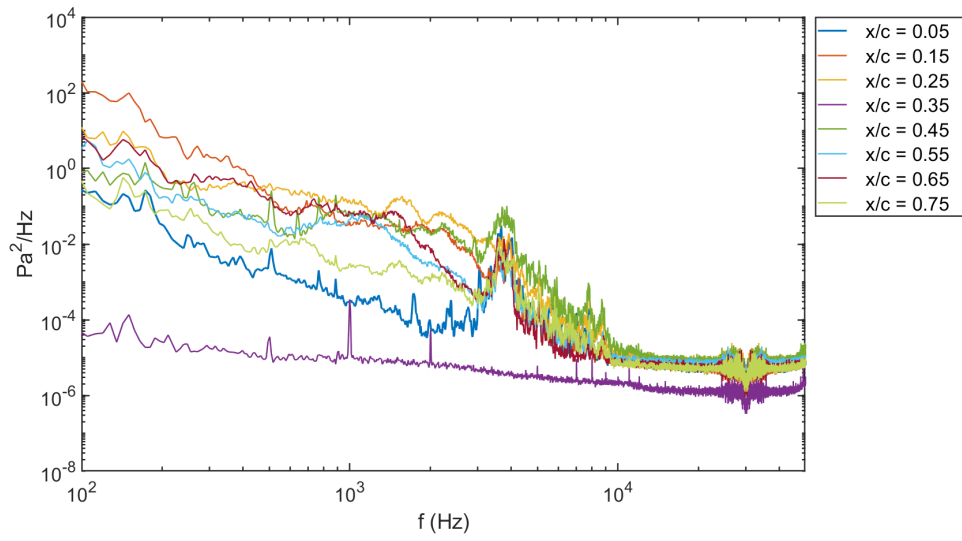


Figure 4.11: Fluctuating power spectra at $5^\circ 10 \frac{m}{s}$, $Re = 0.5102 \cdot 10^5$ - Front

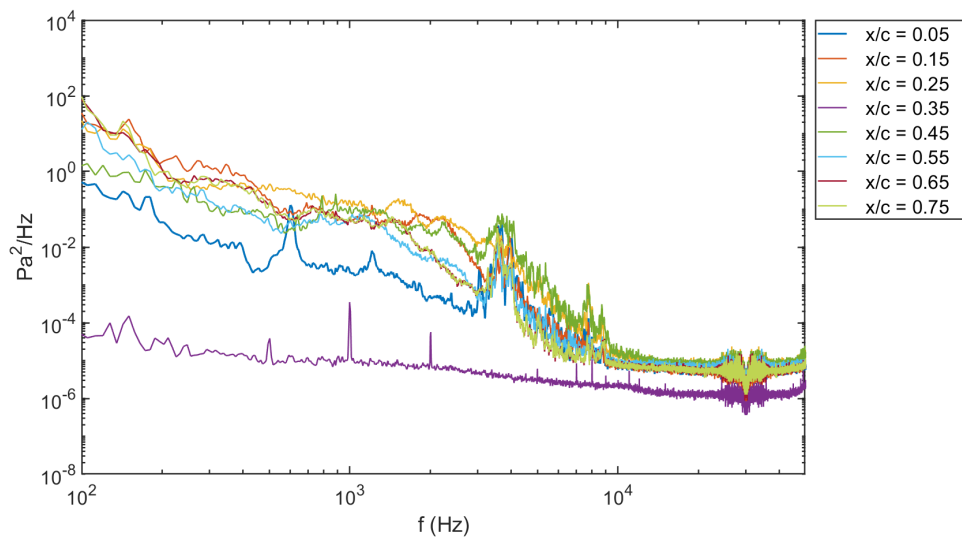


Figure 4.12: Fluctuating power spectra at $10^\circ 10 \frac{m}{s}$, $Re = 0.5102 \cdot 10^5$ - Front

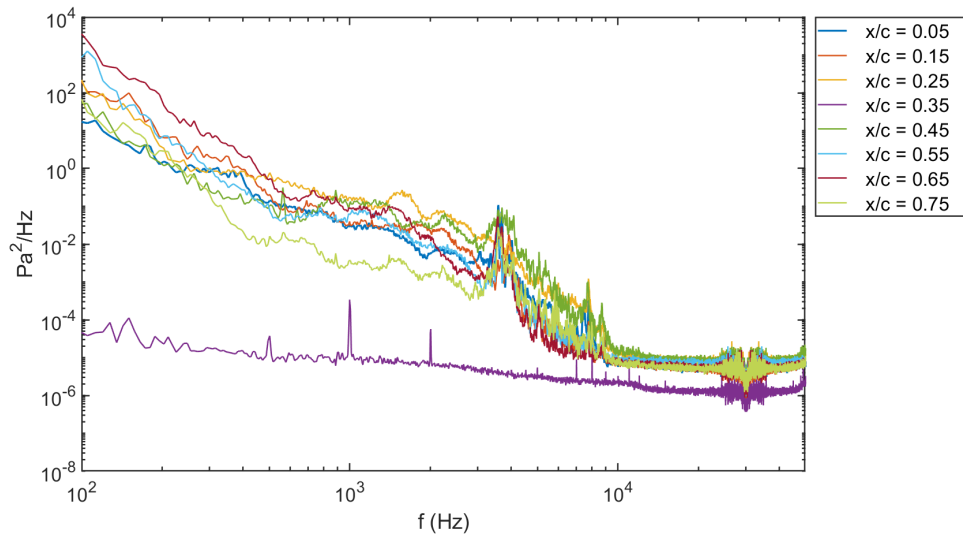


Figure 4.13: Fluctuating power spectra at $15^\circ 10 \frac{m}{s}$, $Re = 0.5102 \cdot 10^5$ - Front

An analysis of the power spectra as a function of Strouhal number allows for comparisons with free field acoustic measurements taken of similar flows. Examining the results presented below in figure 4.14, it can be seen that the Strouhal number of the peaks observed above correspond with the Strouhal number of the dominant tip noise contribution observed by Moreau et al. [7].

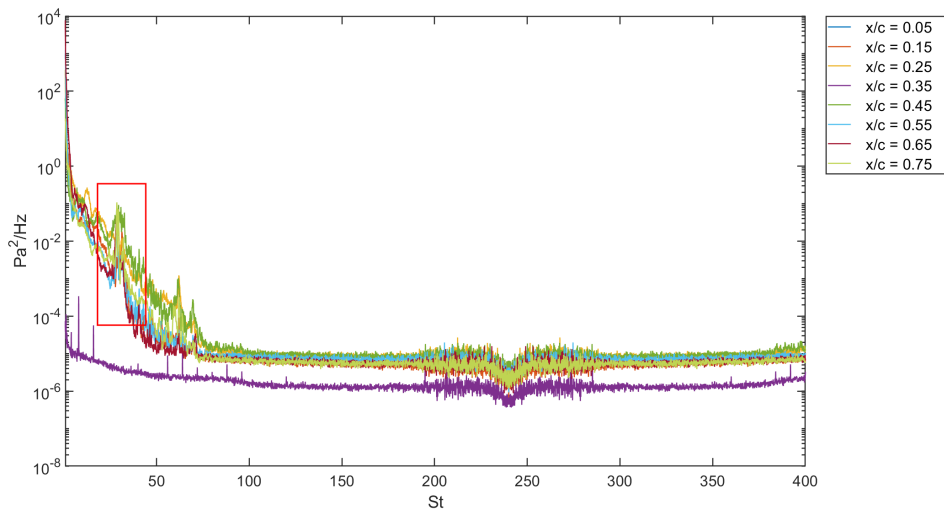


Figure 4.14: Power spectra as a function of Strouhal number at $15^\circ 10 \frac{m}{s}$, $Re = 0.5102 \cdot 10^5$ - Front. Note the region highlighted is the region that represents the local peaks observed above in figures 4.10 to 4.13.

In addition to the power spectra themselves, looking at the normalised RMS power is worthwhile. In order to do this, the power spectra are integrated over the desired frequency range:

$$\text{mean}(g^2) = \int_{f_{min}}^{f_{max}} G(\omega) d\omega \quad (4.1)$$

f_{min} was set at 100Hz and f_{max} was set at $5 \cdot 10^4$ Hz in order to eliminate background noise (both electrical and acoustic) in order to better isolate the flow phenomena of interest.

The square root of the result is then taken in order to obtain the RMS:

$$\text{RMS} = \sqrt{\text{mean}(g^2)} \quad (4.2)$$

An example of the RMS of the power spectra at 10m/s , $Re = 1.531 \cdot 10^5$ is given below in figure 4.15 in which the RMS has been normalised with respect to q_∞ .

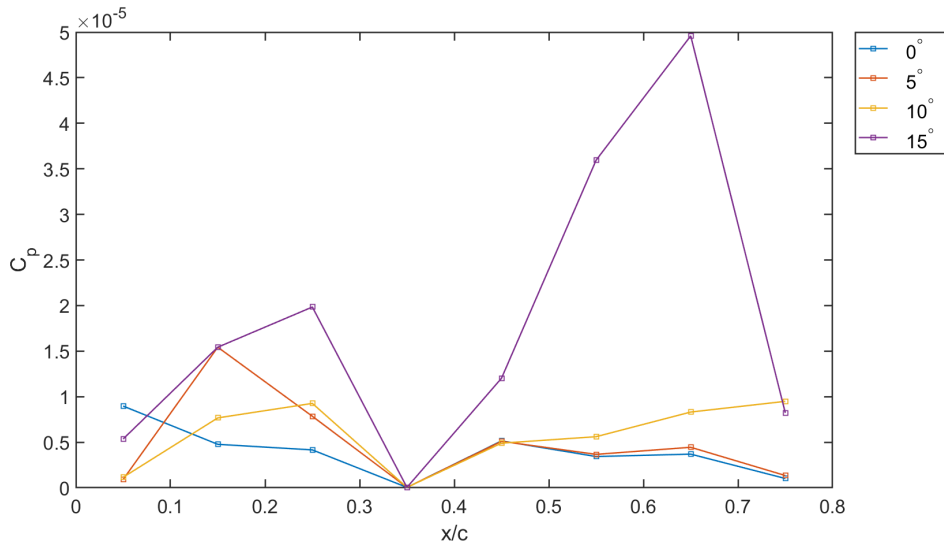


Figure 4.15: C_p vs x/c α sweep at, $Re = 1.531 \cdot 10^5$.

Of particular interest, is the steadily increasing C_p along with α . This can be said to be related to the increases in the axial component of the vortex flow as observed by Birch et al [24].

Chapter 5

Conclusion

Mean and fluctuating pressure measurements have been gathered near the tip of a squared-off NACA 0012 airfoil. Regions of mean pressure instability have been observed within front half (chord-wise) of the airfoil. Relationships between the pressure measured, and macro level results observed in the literature have been drawn, specifically within the vortex roll-up region. Although limited literature exists on this category of data, these results can form the basis of further work investigating the flow physics of wingtip vortex formation and roll-up. Potential repeatability issues have also been noted, however further investigation will be required in order to determine whether or not non-repeatability of mean-pressure data gathering is an unavoidable feature of this particular flow. Fluctuating pressure power spectra were also examined, with relationships between higher frequency peaks and far-field acoustic measurements were drawn. Examining the normalised RMS signals also allowed for a potential link to be drawn between mean fluctuating pressure output and macro-level phenomena observed in literature.

5.1 Future Work

There is a lot of potential to build upon the work performed in this investigation, both within the realm of experimental work and numerical/CFD work. Within the area of experimental work, a higher fidelity set of measurements (higher pressure tap number density) over a similar set of Reynolds numbers and angles of attack would be of benefit. This would allow for better comparisons with theoretical values, and allow for an even better understanding of wingtip vortex flow physics. This would be of particular benefit when it comes to the unsteady pressure measurements, as it would allow for confirmation and/or refinement of the understanding gained regarding the ‘muffling’ effect observed at $x/c = 0.35$. Additionally, an extension of this study that investigates higher Reynolds numbers would allow for relationships to be drawn between unsteady pressure measurements at the surface of the tip, and free-field acoustic measurements taken of that same region (e.g. the study conducted by Moreau et al. [7]). Concurrent flow visualisation investigations will also allow for more conclusive relationships to be drawn between surface pressure and vortex formation and roll up. In terms of CFD investigations, the results of this work can be used as a validation source for simulations that model the flow physics of the region of concern. Given the complexity of the flow within the tip region, LES simulations would likely be the most appropriate starting point, after which, more computationally efficient methods can be investigated.

Bibliography

- [1] D. Birch, T. Lee, F. Mokhtarian, and F. Kafyeke, “Structure and induced drag of a tip vortex,” *Journal of Aircraft*, vol. 41, pp. 1138–1145, sep 2004.
- [2] M. Hollander, “Wingtip pressure distribution measurements and relations with tip-vortex generation: Mid-year progress report,” 2017.
- [3] P. R. Spalart, “Airplane trailing vortices,” *Annual Review of Fluid Mechanics*, vol. 30, no. 1, pp. 107–138, 1998.
- [4] M. R. Fink, “Airframe noise prediction method,” techreport, The Federal Aviation Administration, 1977.
- [5] B. Storms, T. Takahashi, C. Horne, J. Ross, R. Dougherty, and J. Underbrink, “Flap-tip treatments for the reduction of lift-generated noise,” technical memorandum, Ames Research Center, National Aeronautics and Space Administration (NASA), 03 1996.
- [6] T. F. Brooks and M. A. Marcolini, “Airfoil tip vortex formation noise,” *AIAA Journal*, vol. 24, pp. 246–252, feb 1986.
- [7] D. J. Moreau and C. J. Doolan, “An experimental study of airfoil tip vortex formation noise,” in *Proceedings of ACOUSTICS*, 2016.
- [8] S. C. Crow, “Stability theory for a pair of trailing vortices,” *AIAA journal*, vol. 8, no. 12, pp. 2172–2179, 1970.
- [9] G. Batchelor, “Axial flow in trailing line vortices,” *Journal of Fluid Mechanics*, vol. 20, no. 4, pp. 645–658, 1964.
- [10] J. R. Spreiter and A. H. Sacks, “The rolling up of the trailing vortex sheet and its effect on the downwash behind wings,” *Journal of the Aeronautical Sciences*, vol. 18, no. 1, pp. 21–32, 1951.
- [11] H. Chevalier, “Flight test studies of the formation and dissipation of trailing vortices,” *Journal of Aircraft*, vol. 10, pp. 14–18, jan 1973.

- [12] F. Albano, F. D. Gregorio, and A. Ragni, “Trailing vortex detection and quantitative evaluation of vortex characteristics by PIV technique,” in *20th International Congress on Instrumentation in Aerospace Simulation Facilities, 2003. ICIASF 03.*, IEEE, 2003.
- [13] R. Stuff, “The near-far field relationship of vortices shed from transport aircraft,” in *19th AIAA Applied Aerodynamics Conference*, American Institute of Aeronautics and Astronautics, jun 2001.
- [14] A. J. BILANIN, M. E. TESKE, and G. WILLIAMSON, “Vortex interactions and decay in aircraft wakes,” *AIAA Journal*, vol. 15, pp. 250–260, feb 1977.
- [15] J.-U. Klar, C. Breitsamter, S. Hickel, and N. Adams, “Integrated experimental-numerical analysis of high-agility aircraft wake vortex evolution,” *Journal of Aircraft*, vol. 48, pp. 2050–2058, nov 2011.
- [16] E. A. Anderson and T. A. Lawton, “Correlation between vortex strength and axial velocity in a trailing vortex,” *Journal of aircraft*, vol. 40, no. 4, pp. 699–704, 2003.
- [17] K. Q. Zaman, A. F. Fagan, and M. R. Mankbadi, “Experimental study of tip vortex flow from a periodically pitched airfoil section,” in *54th AIAA Aerospace Sciences Meeting, AIAA SciTech, (AIAA 2016-1846)*, 2016.
- [18] V. R. Corsiglia, R. G. Schwind, and N. A. Chigier, “Rapid scanning, three-dimensional hot-wire AnemometerSurveys of wing-tip vortices,” *Journal of Aircraft*, vol. 10, pp. 752–757, dec 1973.
- [19] J. N. Nielsen and R. G. Schwind, “Decay of a vortex pair behind an aircraft,” in *Aircraft Wake Turbulence and Its Detection*, pp. 413–454, Springer US, 1971.
- [20] D. Ciffone and K. Orloff, “Far-field wake-vortex characteristics of wings,” in *7th Fluid and PlasmaDynamics Conference*, American Institute of Aeronautics and Astronautics, jun 1974.
- [21] J. D. Iversen, “Correlation of turbulent trailing vortex decay data,” *Journal of Aircraft*, vol. 13, pp. 338–342, may 1976.
- [22] M. Evans, “Vortex wakes behind high-lift wings,” in *Astrodynamics Conference*, American Institute of Aeronautics and Astronautics, aug 1969.
- [23] M. S. Francis and D. A. Kennedy, “Formation of a trailing vortex,” *Journal of Aircraft*, vol. 16, pp. 148–154, mar 1979.
- [24] T. Lee and J. Pereira, “Nature of wakelike and jetlike axial tip vortex flows,” *Journal of Aircraft*, vol. 47, pp. 1946–1954, nov 2010.

- [25] J. S. Chow, G. G. Zilliac, and P. Bradshaw, “Measurements in the near-field of a turbulent wingtip vortex,” tech. rep., NASA, 1993.
- [26] R. B. G. Michea Giuni, “Vortex formation on squared and rounded tip,” *Aerospace Science and Technology*, March 2013.
- [27] M. Ramasamy, B. Johnson, and J. G. Leishman, “Turbulent tip vortex measurements using dual-plane stereoscopic particle image velocimetry,” *AIAA journal*, vol. 47, no. 8, p. 1826, 2009.
- [28] J. Walker, H. Helin, and D. Chou, “Unsteady surface pressure measurements on a pitching airfoil,” tech. rep., American Institute of Aeronautics and Astronautics, mar 1985.
- [29] J. B. McDevkt and A. F. Okun, “Static and dynamic pressure measurements on a naca 0012 airfoil in the ames high reynolds number facility,” techreport NASA-TP-2485, NASA Ames Research Center, NASA Ames Research Center; Moffett Field, CA, United States, 1985.
- [30] O. Kandil, T.-C. Wong, I. Adam, and C. Liu, “Prediction of near- and far-field vortex-wake turbulent flows,” in *20th Atmospheric Flight Mechanics Conference*, American Institute of Aeronautics and Astronautics, aug 1995.
- [31] N. Insturments, “Pxi systems,” 2017.
- [32] W. B. R. David R. Englund, *The Infinite Line Pressure Probe*. NASA, 1984.
- [33] M. Awasthi, *Sound Radiated from Turbulent Flow over Two and Three-Dimensional Surface Discontinuities*. PhD thesis, Virginia Institute of Technology, 2015.
- [34] M. Drela, “xfoil (software).” executable software package, December 2013.
- [35] M. Drela and H. Youngren, “General description,” November 2001. (Accessed on 05/14/2018).

Appendix A

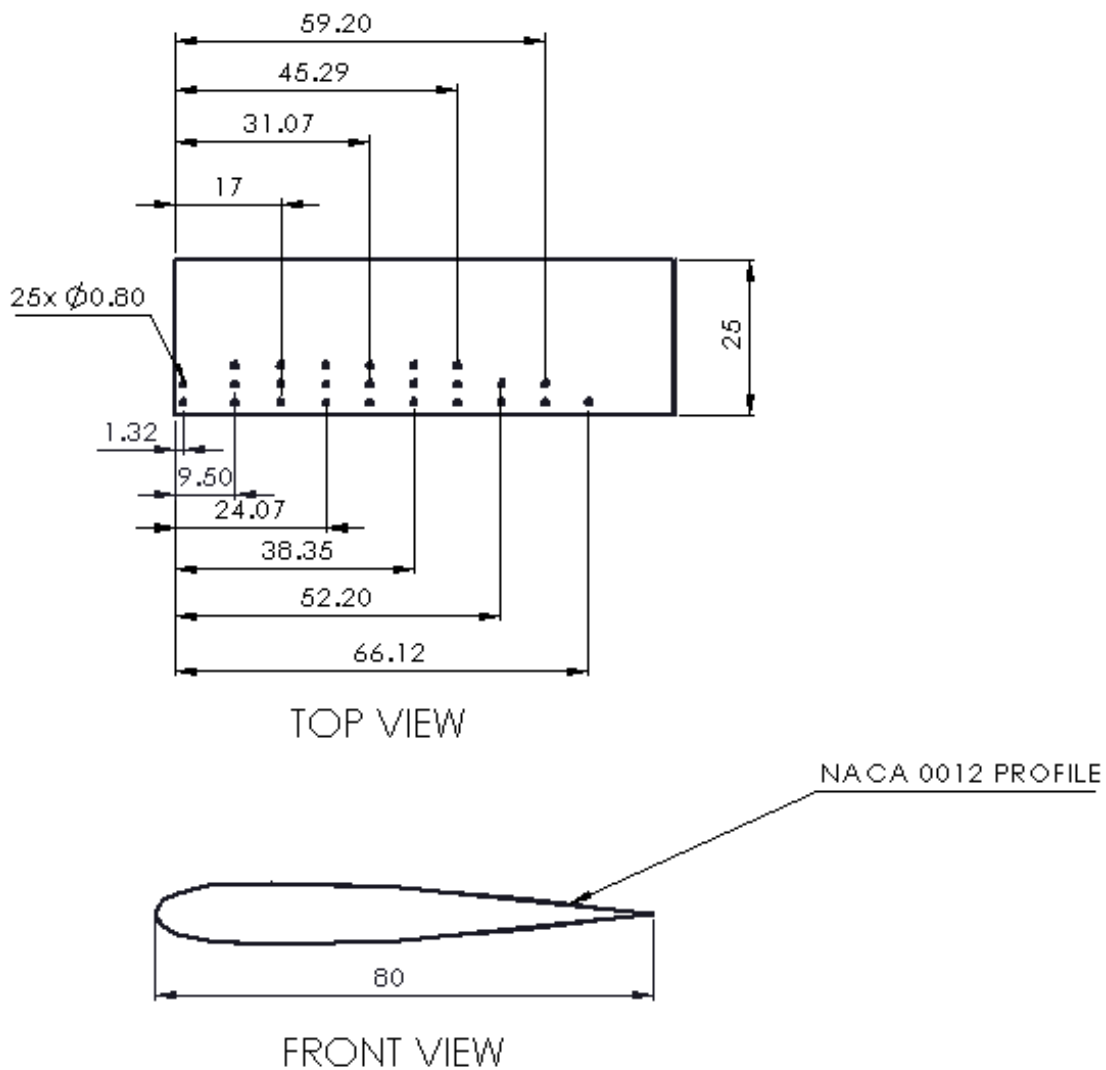


Figure A.1: Detailed drawing of tip attachment with taps on top surface. All dimensions in mm unless otherwise specified. Drawing not to scale.

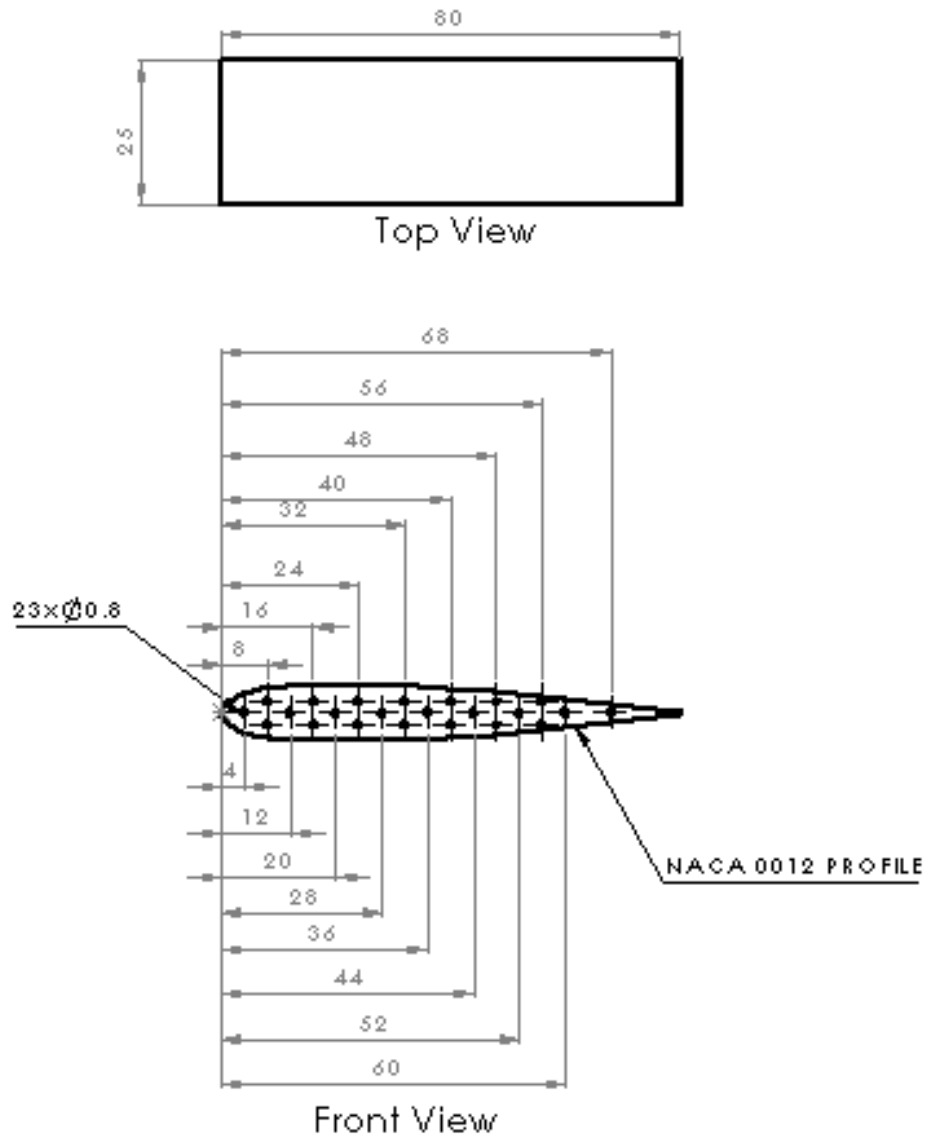


Figure A.2: Detailed drawing of tip attachment with taps on front surface. All dimensions in mm unless otherwise specified. Drawing not to scale.

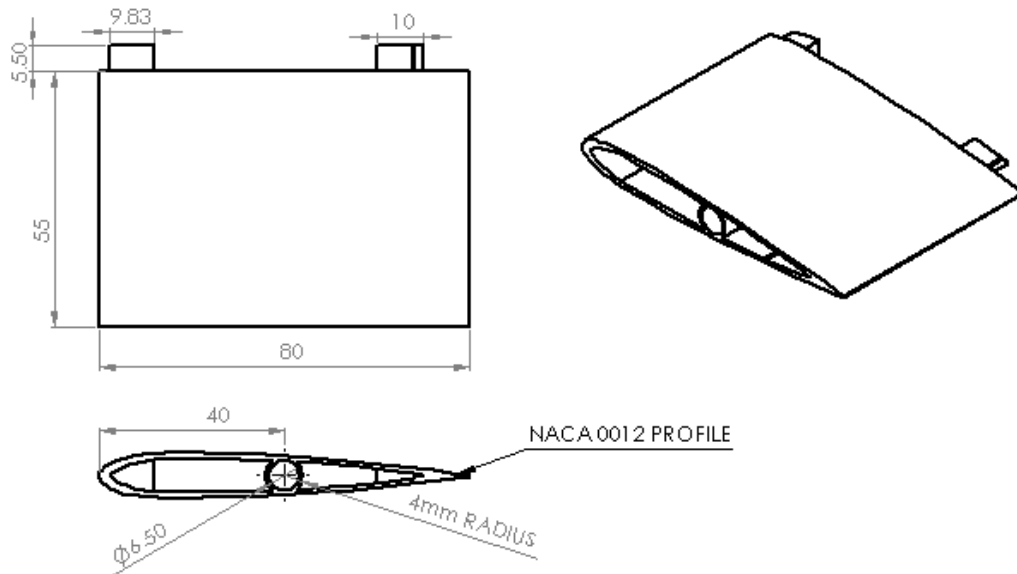


Figure A.3: Detailed drawing of model base. All dimensions in mm unless otherwise specified. Drawing not to scale.

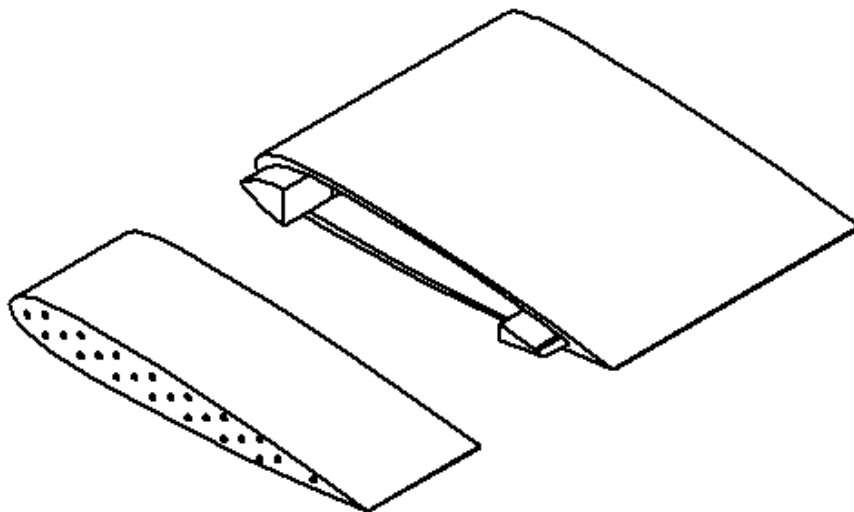


Figure A.4: Exploded view drawing of assembly of front tip attachment with base. Drawing not to scale.

Appendix B

This section contains the MATLAB code used within the analysis conducted in the above investigation. Personal directory information has been removed.

B.1 MATLAB code used to gather and analyse mean pressure data

```
while(1)
    tic
    stag_port = 1; %total pressure port
    stat_port = 2; %static pressure port
    R = 287;
    T = 299.6; %Ambient Temp
    patm = 101325;%Ambient Pressure
    rho = patm./(R*T); %Density
    pMean = scanivalveMeasure(scani, scaniSample);
    dp = pMean(stag_port)-pMean(stat_port);
    V = sqrt(abs(2*dp/rho))
    if dp < 0;
        V = 'Error';
    t =toc;
    end
end

Tap1 = pMean(3);
Tap2 = pMean(4);
Tap3 = pMean(5);
Tap4 = pMean(6);
Tap5 = pMean(7);
Tap6 = pMean(8);
Tap7 = pMean(9);
```

```

Tap8 = pMean(10);
Tap9 = pMean(11);
Tap10 = pMean(12);
Tap11 = pMean(13);
Tap12 = pMean(14);
Tap13 = pMean(15);
Tap14 = pMean(16);
dp = pMean(stag_port)-pMean(stat_port);
V = sqrt(2*dp/rho);
T_C=28;
T=T_C+273;

```

B.2 MATLAB code used to compute and plot the RMS values of the spectral data

```

q_inf=0.5*1.225*(10^2);
RMS1_15deg=sqrt(trapz(0:(mic1(6668)/6654):mic1(6668),mic1(14:6668)));
RMS2_15deg=sqrt(trapz(0:(mic2(6668)/6654):mic2(6668),mic2(14:6668)));
RMS3_15deg=sqrt(trapz(0:(mic3(6668)/6654):mic3(6668),mic3(14:6668)));
RMS4_15deg=sqrt(trapz(0:(mic4(6668)/6654):mic4(6668),mic4(14:6668)));
RMS5_15deg=sqrt(trapz(0:(mic5(6668)/6654):mic5(6668),mic5(14:6668)));
RMS6_15deg=sqrt(trapz(0:(mic6(6668)/6654):mic6(6668),mic6(14:6668)));
RMS7_15deg=sqrt(trapz(0:(mic7(6668)/6654):mic7(6668),mic7(14:6668)));
RMS8_15deg=sqrt(trapz(0:(mic8(6668)/6654):mic8(6668),mic8(14:6668)));
RMSx=[0 5 10 15]);
RMS0_deg = ([RMS1_0deg RMS2_0deg RMS3_0deg RMS4_0deg RMS5_0deg RMS6_0deg
RMS7_0deg RMS8_0deg]/q_inf);
RMS5_deg = ([RMS1_5deg RMS2_5deg RMS3_5deg RMS4_5deg RMS5_5deg RMS6_5deg
RMS7_5deg RMS8_5deg]/q_inf);
RMS10_deg = ([RMS1_10deg RMS2_10deg RMS3_10deg RMS4_10deg RMS5_10deg
RMS6_10deg RMS7_10deg RMS8_10deg]/q_inf);
RMS15_deg = ([RMS1_15deg RMS2_15deg RMS3_15deg RMS4_15deg RMS5_15deg
RMS6_15deg RMS7_15deg RMS8_15deg]/q_inf);

plot(x,RMS0_deg,'-s','Linewidth',1.5);
%xticks([0 5 10 15])
xlabel('x/c','FontSize',20);
ylabel('C_p','FontSize',20);
%xlim([0 20])
set(gca, 'FontSize', 20,'LineWidth',1.5);

```

```
set(gcf, 'Units', 'Normalized', 'OuterPosition', [0 0 1 1]);
hold on
plot(x,RMS5_deg,'-s','Linewidth',1.5);
plot(x,RMS10_deg,'-s','Linewidth',1.5);
plot(x,RMS15_deg,'-s','Linewidth',1.5);
h1=legend('{ }0^\circ{ }','{ }5^\circ{ }','{ }10^\circ{ }',
'{ }15^\circ{ }','location','northeastoutside')
set(h1,'FontSize',20);
hold off
```

Appendix C

C.1 y/c sweep data near the tip region

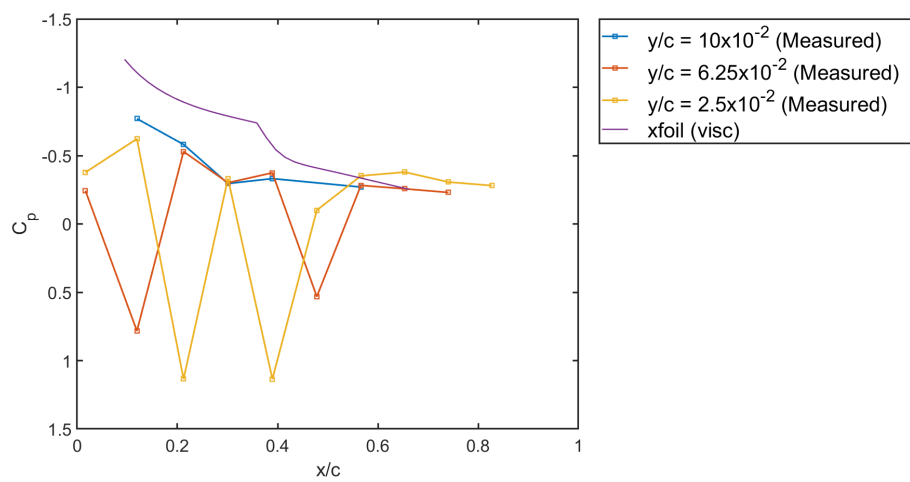


Figure C.1: y/c sweep at $20 \frac{m}{s}$, $Re = 1.204 \cdot 10^5$ - Suction Side

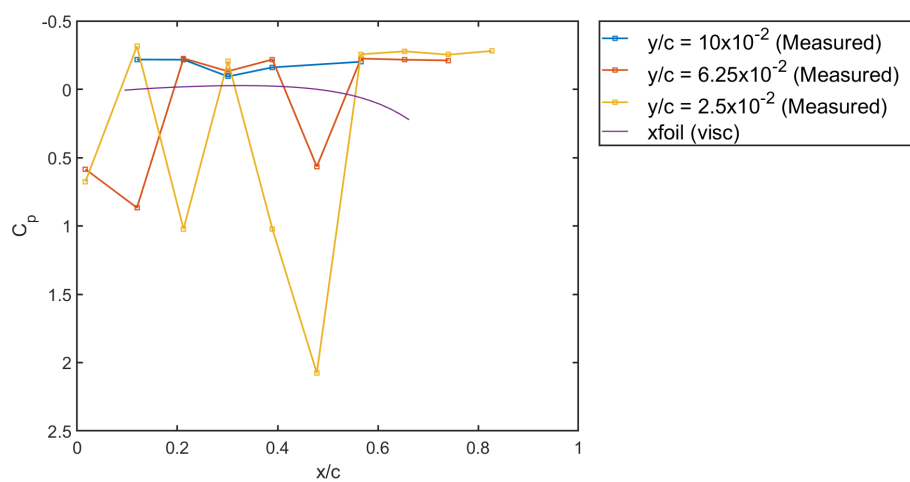


Figure C.2: y/c sweep at $20 \frac{m}{s}$, $Re = 1.204 \cdot 10^5$ - Pressure Side